## Feasibility Study and Design of Soft-catcher for Damaged Concrete Debris

Kwee Siang Ong<sup>1</sup>

<sup>1</sup>Delft University of Technology, The Netherlands

#### **Abstract**

The main thrust to initiate this research work emerges from the need to enhance prediction capabilities in explosive safety of ammunition magazine. Debris launch information, such as mass distribution, is vital for hazard assessment and to calibrate numerical models that simulate concrete structure breakup. The current technique to collect explosively-damaged debris after test execution does not yield representative test data on the launch condition. This research work explores the use of polymeric foam, Rohacell 110WF, as the benchmark material for soft-catcher to trap concrete debris at close distance, without inducing additional damage.

One-dimensional (1-D) shock wave models to predict crushing responses of cellular foam material are briefly reviewed. From which, the rigid-power law hardening (R-PLH) model has been selected. Modifications to the existing R-PLH model are proposed to incorporate effects of debris nose geometry, frictional resistance and initial elasticity of the foam material. Analytical predictions of a representative impactor-target scenario, using both R-PLH Model and Modified-R-PLH Model, are performed with various impact velocities. It is concluded that the Modified R-PLH Model exhibits reductions in shock-induced stresses and strains, as compared to R-PLH Model. This is primarily due to decrease in particle velocity jump across shock wave front as the Modified R-PLH Model considers non-zero particle velocity in the uncrushed region. Consequently, the Modified R-PLH Model predicts slower deceleration of debris motion. The Modified-R-PLH Model eventually establishes the preliminary design length of the soft-catcher. High-fidelity finite element tool, LS-DYNA, is utilised to perform numerical analyses. 1-D numerical analyses with 20 m target length have verified various assumptions adopted in the Modified R-PLH Model. Good agreement of debris velocities, shockinduced stresses and strains are observed. Two different debris velocity time response regimes that relate to plastic and elastic wave propagations are identified, in which the drawback of Modified-R-PLH Model is discussed. The 1-D numerical model is redeveloped using 2 m target length to include the effect of design length for the soft-catcher. Following then, 2-D numerical models are created to study how the tensile and shear failure stresses of the foam material can influence the interaction between debris and soft-catcher. Furthermore, sensitivity of shear and tensile failure stresses of foam material on the overall soft-catcher design are also evaluated. Lastly, these results obtained from 2-D analyses are translated into design considerations for the soft-catcher. Charts are also plotted to facilitate design of soft-catcher with different debris launch velocities.

#### 1. Introduction

Ammunition storage magazines are always subjected to a potential risk of accidental explosion, in which effects can be devastating to the surrounding environment. The main causes of human lethality in such confined explosion are primarily due to blast pressure and debris throw hazards. Mitigation against these explosive effects has always been a key focus in research development of explosive safety. The Klotz Group (KG) has a particular interest

<sup>&</sup>lt;sup>1</sup> The Klotz Group (KG) is a committee that comprises international subject-matter-experts on explosive safety, has strong interest in investigating debris throw hazard arising from accidental explosion of ammunition magazine structure.

in dealing with debris throw hazards. During 2007 and 2008, TNO Defence, Security and Safety and Fraunhofer Ernst-Mach-Institute (EMI) had jointly developed the semi-empirical KG Software that computes debris throw distances and predicts debris energies along its ballistic path, which can be used for risk analysis and evaluation. Nevertheless, there are still limitations in this software to accurately predict the breakup of concrete structures and model the disintegration of debris upon impact with ground. Obtaining debris data at launch condition such as mass distribution, residual damage level etc. will also be very useful to calibrate numerical models that simulate concrete breakup process. The current practice is to collect debris at resting condition (i.e. post-test retrieval) which does not yield representative data, considering that debris may disintegrate further due to collision with other flying debris during its ballistic flight and especially due to impact with the ground surface. Hence, this motivates the current research to explore feasible solution to "soft-catch" explosively-damaged debris at initial launch condition. The guiding principles behind the feasibility study include ensuring minimal damage to the debris during soft-catching process and ability to terminate debris motion within stipulated distance.

Getting information such as debris launch velocity, sizes and damage level is a prerequisite before exploring feasible soft-catch solutions. KG has previously conducted explosive trials to study the breakup of KASUN structure; an above-ground ammunition storage magazine. The KASUN, which is considered as the reference structure in this research study, has an internal cubicle dimension of 2 m by 2 m by 2 m, with wall and roof thickness of 0.15 m. In 2005, a series of clamped reinforced concrete slab tests were carried out in the Ballistic Laboratory of TNO to study the breakup of one-way slabs under explosive loading [1]. A steel-composite explosion box was used to clamp the slab specimens, as illustrated in Figure 1-1. The loading densities tested range from 0.5 kg/m³ to 4 kg/m³. As it is deem viable to re-use the explosion box for the future soft-catcher test, the dimension of this explosion box is taken into consideration when sizing up the soft-catcher.

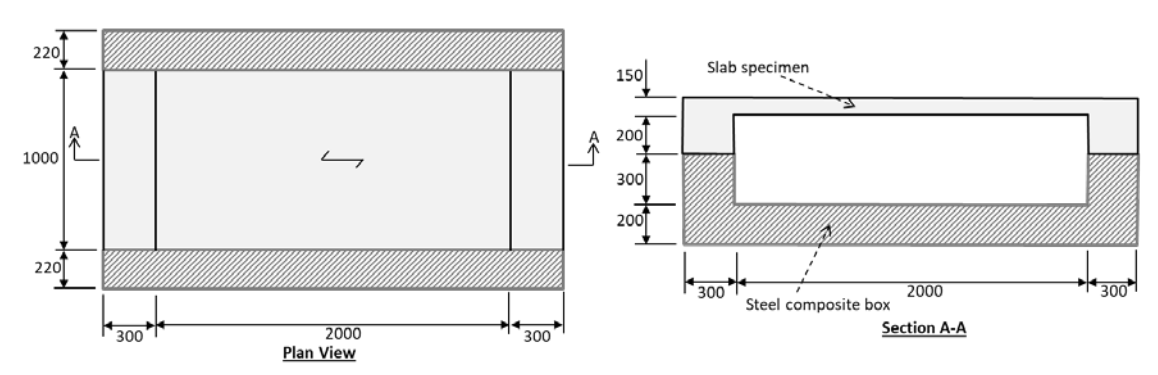


Figure 1-1: Plan and section view of clamp RC slab test setup [1]

This thesis research primarily studies the feasibility of using foam material to decelerate debris moving at various launch velocities, leveraging on analytical prediction models and computational analyses. Parameters such as debris penetration distances, impact stresses acting on the debris and boundary support reactions are extensively evaluated for the purpose of designing a soft-catcher. Specific research questions that are addressed include:

- What is the design length of soft-catcher?
- What are the impact stresses on the debris compared with the design strength of applied concrete and residual strength of damaged debris?
- What are the magnitudes of reaction forces at boundary supports of soft-catcher?

The outline of the paper, which also reflects the approach to the research, is as follows. First, specific requirements of soft-catcher are identified to select a suitable foam type as benchmark material. The impact scenario to be considered for the feasibility study is established. The shock-wave theories related to foam materials are reviewed, in which an improved one-dimensional (1-D) analytical model is introduced to perform first order design for the soft-catcher. Numerical simulations using LS-DYNA are performed to verify analytical model predictions. As the 1-D analytical model assumes infinite length of softcatcher, the effects arising from end boundary conditions of soft-catcher are brought into attention using numerical analyses. Moving on, the 1-D numerical models are propagated into two-dimensional (2-D) space domain in order to further evaluate design parameters of softcatcher, under the influences of shear and tensile resistances. The resultant material responses are compared with 1-D model predictions. Sensitivity studies of shear and tensile failure stresses within the soft-catcher are performed to examine its effects on overall soft-catcher responses. Design charts for soft-catcher are subsequently presented over a range of debris launch velocities. The research works are eventually concluded and possible areas of focus for future research efforts are recommended.

## 2. Specific Requirement of Soft-Catcher Material

It is vital for soft-catcher material to indent and tear apart easily at first instance of impact, without inducing considerably high resistance. The material must have good energy absorption capability such that penetrating debris can decelerate effectively. Cellular foam materials such as polymeric foams are commonly used as impact energy absorbers in various engineering application. It has a low yield stress and strain which allows ease of penetration at first instance of impact. The long and relatively stable yield stress plateau allows large deformation at almost constant stress, which provides high crushability to dissipate impact energies. A typical quasi-static compressive stress-strain curve of a cellular foam material is shown in Figure 2-1. In this research, commercially-available foam known as Rohacell 110WF, with a nominal density of 110 kg/m3, will be considered as benchmark material for soft-catcher. Arezoo in [2] investigated the quasi-static mechanical properties of Rohacell foams, with densities ranging from 50 kg/m3 to 200 kg/m3. Table 2-1 presents some of the measured material properties for the various foams tested. The Poisson Ratio (PR) for this foam material is taken as zero in this research work, as Arezoo in [2] had reported that negligible lateral strain was observed during the material testing.

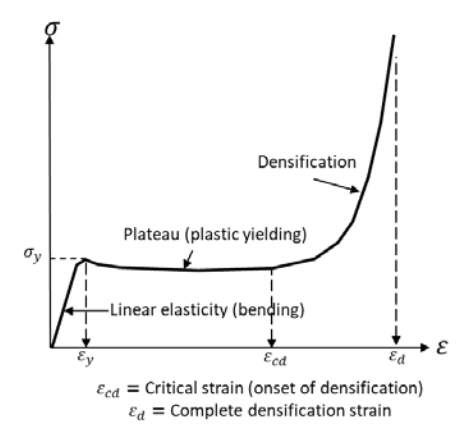


Figure 2-1: Typical compressive constitutive curve for elasto-plastic foam material

Foam Material	Density (kg/m <sup>3</sup> )	$\mathcal{E}_{\mathrm{y}}$	E <sub>c</sub> (MPa)	$\sigma_{pl}$ (MPa)	$\sigma_{yt}$ (MPa)	$\sigma_{ft} \\ (MPa)$	$\tau_{ft} \\ (MPa)$
Rohacell 51WF	51	0.0286	32.5	0.93	1.2	1.44	0.75
Rohacell 71WF	71	0.0287	48.5	1.39	1.64	1.75	1.04
Rohacell 110WF	110	0.0286	82.5	2.36	2.05	2.17	1.86
Rohacell 200WF	200	0.0369	246.5	9.1	5.7	7.71	4.94

Table 2-1: Measurement of quasi-static material properties for various Rohacell foams tested by Arezoo [2]

#### 2.1. Impact Scenario for Consideration

Both the clamped slab tests in [1] and the ballistic filtering phenomenon reported by the KG has indicated that at close distance to explosion, the entire concrete wall will initially launch at approximately the same velocity that is equal to Debris Launch Velocity (DLV) in [3]. As the debris cloud expands further, the effect of ballistic coefficient for individual debris increases such that debris with larger masses will move faster than the smaller debris masses.

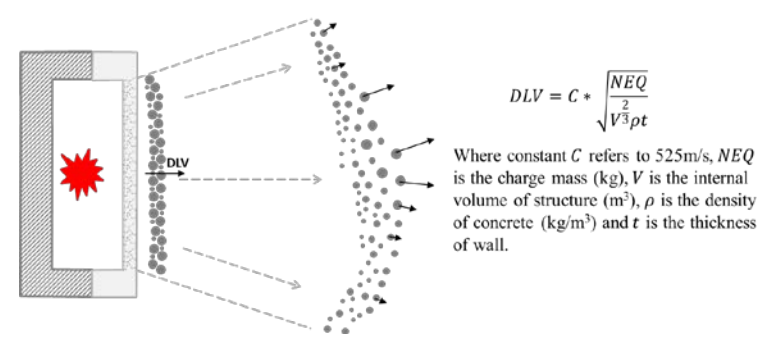


Figure 2-2: Ballistic filtering phenomenon after break-up of concrete wall

Considering the complexities involved in evaluating soft-catcher's response when subjected to multiple hits of debris moving in the debris cloud at different velocities, this research work will therefore focus on impact scenario in which the entire concrete wall moves at its initial debris launch velocity. This implies that the soft-catcher will catch the debris at close distance such that the overall debris surface remains plane (See Figure 2-2). Three debris launch velocities of 50 m/s, 100 m/s and 145 m/s will be evaluated. These velocities correspond to the loading density<sup>2</sup> of 1.7 kg/m<sup>3</sup>, 6.8 kg/m<sup>3</sup> and 14.3 kg/m<sup>3</sup> respectively, using DLV formula. The highest velocity of 145 m/s is taken as the design debris launch velocity for the soft-catcher. Other input parameters, which are consistent with the KASUN structure (ammunition magazine structure) [4] include: internal structure volume of 8 m<sup>3</sup> (i.e. 2 m by 2 m by 2 m) and wall thickness of 0.15 m. The concrete density is assumed to be 2500 kg/m<sup>3</sup>.

<sup>2</sup> The KASUN III trials conducted in 2009 considered loading densities that range from 0.816 kg/m3 to 13.06 kg/m3.

#### 3. Feasibility Study and Design (Stage 1) – Analytical Predictions

#### 3.1. Shock Wave Models

The overall resistance force to debris penetration primarily comprises the plastic crushing force of the cellular material, dynamic force, tearing force (i.e. tensile and shearing fractures during penetration in cellular material) and the friction force between the debris and the cellular material (See Figure 3-1).

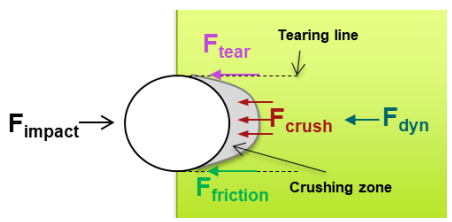


Figure 3-1: Resultant forces resisting debris penetration in cellular material

Particularly, dynamic stress enhancement and localization of cell crushing in the region between the impactor (i.e. debris) and the shock wave front are two prominent characteristics of shock compression in cellular solids [5] [6] [7]. With sufficiently high impact velocity, a plastic shock wave can be induced to propagate ahead of the debris. This shock wave front refers to the interface separating crushed and uncrushed cells under dynamic compression. In this respect, the debris-penetration problem discussed in this paper will assume that the shock wave is propagating at a subsonic speed (i.e. velocity of wave front lower than the linear sound velocity of stress wave in the material). This also implies that a precursor elastic wave will propagate ahead of the shock wave, at the speed of the linear sound velocity.

In this feasibility study, the approach to derive analytical solutions is based on a 1-D shock wave model. In this 1-D shock wave model, it is assumed that there is no change in cross-section area of the 1-D material. The Rankine-Hugoniot relationships that describe the discontinuities in physical quantities of the cellular material across the shock wave front are the fundamental principles behind shock wave models. The main difference between various shock wave models lies in the assumption of material states within two regions (i.e. region A and B as identified in Figure 3-2). Considering that region A and B denote the pre-shock (uncrushed zone) and post-shock (crushed zone) respectively, the jump conditions can be formulated using mass and momentum conservation laws across the shock front.

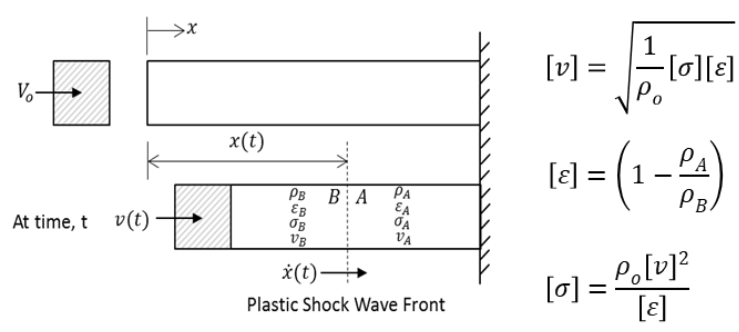


Figure 3-2: Shock wave propagation in one-dimensional cellular material and respective jump conditions, where bracket [ ] indicates the jump in physical quantities

Reid and Peng [5] first proposed a shock wave model to predict the crushing strength enhancement in wood specimens, under the assumption of rigid-perfectly plastic-locking (R-

P-P-L) idealization for the material's stress-strain response. This model retained the two main features of the material constitutive curve, namely; plateau stress  $\sigma_{pl}$  and a locking strain  $\varepsilon_L$ . The locking strain in this model is defined as the critical strain to onset of densification (See Figure 3-3). This critical strain is the strain value that corresponds to the peak energy absorption efficiency value for the material [8]. This model assumes that when the precursor elastic wave propagates through, the material is instantaneously stressed up to plateau level (See Figure 3-3), with no increase in material strain. When the plastic shock wave passes through, material strain will jump from zero to locking strain value, and the material stress will increase from plateau stress to shock stress (i.e.  $\sigma_B = \sigma_A + \frac{\rho_o[v]^2}{[\varepsilon]}$ ). This resultant increase in stress for material within the crushed zone (i.e. region B) is computed using the stress jump equation shown in Figure 3-2. Pattofatto [9] subsequently formulated a Power Law Shock Model to improve the R-P-P-L model, by allowing a more realistic definition of the locking strain. Instead of using a fixed value for the locking strain, this model determines the locking strain (i.e. shock strain) based on the initial impact velocity. A power-law equation (i.e.  $\sigma =$  $\sigma_v + k\varepsilon^n$ ) is established to describe the strain hardening regime of the material. This equation combines with stress jump equation (See Figure 3-2) to evaluate the locking strain as function of initial impact velocity. Table 3-1 presents the assumption of material states across shock wave front in R-P-P-L and Power Law Shock Model. It is worthwhile to mention that the shock wave models discussed thus far had assumed a single but different strain value as the locking strain to represent the strain densification regime. In deriving solutions to predict debris penetration distance using these shock wave models, it has to assume that the material states in Table 3-1 remain constant in time. Furthermore, the material stress and strain are also assumed to be constant in spatial domain.

Table 3-1: Assumptions of material states across shock wave front for R-P-P-L and Power Law Model

	R-P	-P-L	Power Law Model			
Model Parameters	Post- shock	Pre- shock	Post-shock	Pre-shock		
Ctmass				σ – σ		
Stress	$\sigma_{\!B}$	$\sigma_{A} = \sigma_{pl}$	$\sigma_B$	$\sigma_{A} = \sigma_{y}$		
Strain	$arepsilon_B = arepsilon_L$	$\varepsilon_A=0$	$\varepsilon_B = \left(\frac{\rho_o V_o^2}{k}\right)^{\frac{1}{n+1}}$	$\varepsilon_A=0$		
Particle Velocity	$v_B = V_o$	$v_A = 0$	$v_B = V_o$	$v_A = 0$		

Most of the cellular foam materials exhibit shock stress and strain reduction as the amplitude of the plastic shock wave reduces over time. The use of single locking strain value to represent material strain in crushed zone will not provide accurate predictions of stress changes across the shock wave front. This is especially the case when the stress changes can be sensitive to the jumps in particle velocity and strain across the shock wave front [9]. Zheng et al. [10] proposed a rigid-power law hardening (R-PLH) idealization model, which is developed based on continuum-based shock wave theory. The R-PLH model considers the changes in shock-induced strains and particle velocity jumps over time, using material constitutive relationship that describes the non-linear strain hardening response of the material. Unlike other idealisation models that generally assume constant stresses within the crushing zone, the R-PLH model includes crushed material behind the shock wave front as part of the mass inertia in its equation of motion. This implies that the R-PLH model explicitly evaluates the shock stresses and strains closely behind the shock wave front. Closed form or semi-closed form general solutions of the physical quantities across the wave front can be derived with three main parameters involved; yield stress  $\sigma_y$ , strength index K and

strain hardening index n. In this study, the R-PLH model is selected as the base model for further modifications presented in Section 3.2. Figure 3-3 presents the stress-strain idealizations for various models.

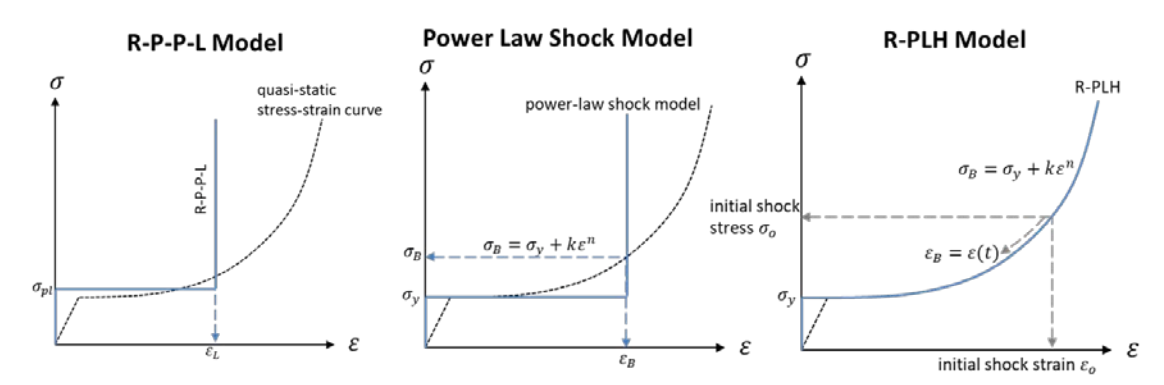


Figure 3-3: Stress-strain idealization for various shock wave models

## 3.2. Modified R-PLH Model

In the R-PLH Model, materials closely behind the shock wave front are subjected to shock-induced stresses and strains. The particle velocities of materials in the crushed zone (i.e. post-shock region) are assumed to be the same as the debris velocities. In the uncrushed zone (i.e. pre-shock region), the material is instantaneously "pre-stressed" up to yielding stress, while the particle velocity and the material strain remain zero. In the interest to improve accuracies of analytical prediction, this research proposes to modify the existing R-PLH Model. These modifications incorporate effects due to different geometries of impactor's nose, in the forms of shape coefficients. It also takes into account the various changes in cellular material states in the pre-shock region, due to the presence of induced elastic wave propagation.

Jones et al. in [11] studied the effect of pressure-dependent friction on the normal impact and penetration problem by a rigid projectile, in which two dimensionless parameters known as the shape coefficients  $N_1$  and  $N_1$  can be derived accordingly. One is referred to **Annex A** for the derivation of these shape coefficients. Chen and Li in [12] had previously included these coefficients into the penetration resistance, when formulating the equation of motion. Similarly, these coefficients can be incorporated within the Modified-R-PLH Model (See **Annex B**). As the shape coefficients for debris with plane face are equal to unity, these coefficients  $N_1$  and  $N_1$  are conveniently omitted in the subsequent formulations.

Unlike R-PLH Model, Modified-R-PLH Model considers that the materials within the preshock region reach elastic strain  $\varepsilon_Y$  and that these uncrushed materials are moving at velocity  $v_{A_{initial}}$  due to induced elastic wave. Note that the sequences of formulating the final solutions in Modified-R-PLH Model generally follow the R-PLH Model presented by Zheng [10]. The initial particle velocity can be defined as follows.

$$v_{A_{initial}} = \frac{\sigma_y}{\rho_o c_1} = \varepsilon_Y c_1$$
 where  $c_1$  refers to the linear sound velocity of material (1)

Figure 3-4 shows the constitutive relationship of the Modified-R-PLH Model and the constitutive relations in stress versus plastic strain plot. The plastic strain is evaluated as the total strain minus the elastic yielding strain.

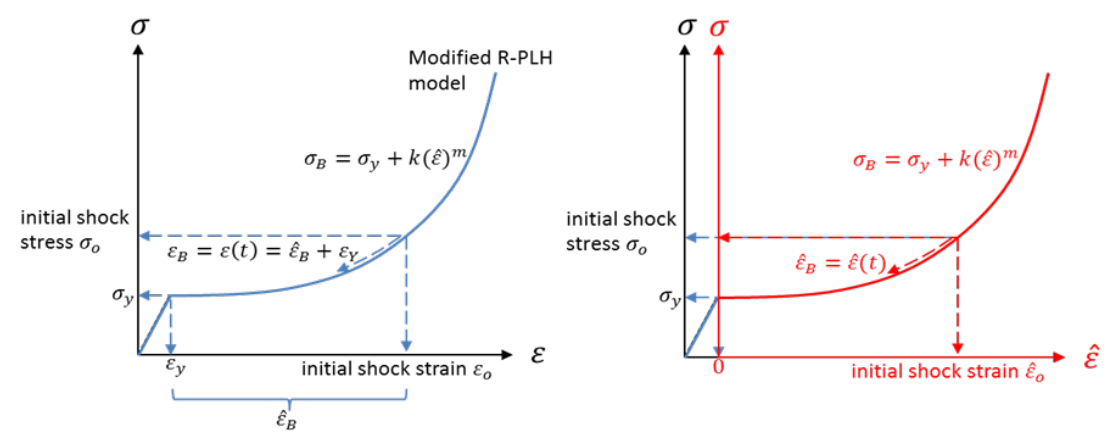


Figure 3-4: Stress-strain idealization for Modified R-PLH Model in  $\sigma$  vs  $\varepsilon$  (left plot) and in  $\sigma$  vs  $\hat{\varepsilon}$  (right plot)

With the various Rankine-Hugoniot jump conditions specified across the wave front (See Figure 3-2), the time derivatives of the relative velocity and strain jumps can be derived accordingly as follows.

$$\frac{d}{dt}(v_B - v_A) = \frac{d}{dt}(v_{Brelative}) = \frac{\frac{1}{2}\left(\sigma'(\hat{\varepsilon}_B) + \frac{\sigma(\hat{\varepsilon}_B) - \sigma_y}{\hat{\varepsilon}_B}\right)\dot{\hat{\varepsilon}_B}}{\rho_o\sqrt{\frac{1}{\rho_o}\left(\frac{\sigma(\hat{\varepsilon}_B) - \sigma_y}{\hat{\varepsilon}_B}\right)}}$$
(2)

The above expression can be further simplified into Eq. (3) with relative shock wave velocity  $\dot{x}$  and the average (i.e.  $k(\hat{\varepsilon}_B)$ ) between the slopes of tangent line at shock state and the Rayleigh line. The relative shock velocity can be determined through mass and momentum conservation conditions across the wave front.

$$\frac{d}{dt}(v_{Brelative}) = \frac{k(\hat{\varepsilon}_B)\dot{\hat{\varepsilon}_B}}{\rho_o \dot{x}} \tag{3}$$

Figure 3-5 illustrates the Rayleigh line which describes the constitutive states of material under the effect of shock impact.

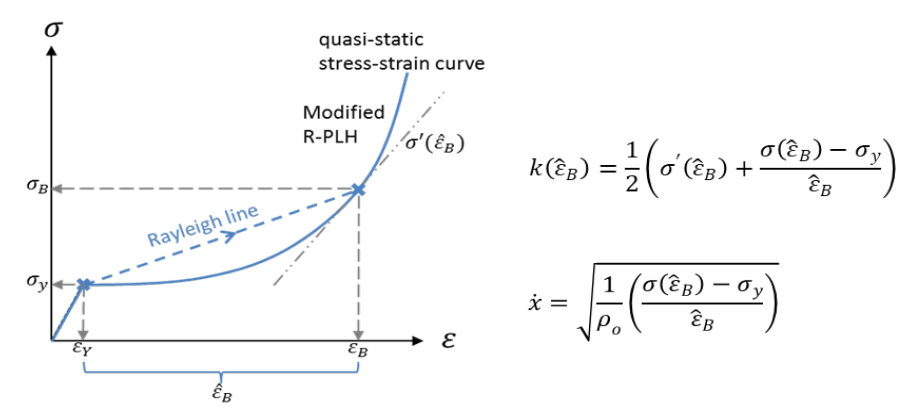


Figure 3-5: Rayleigh line for Modified R-PLH Model

The equation of motion considered for Modified-R-PLH Model can be expressed as follows.

$$\left(M_o + \rho_o A_o x(t)\right) \frac{d}{dt} \left(v_{B_{relative}}\right) = -\sigma^*(\hat{\varepsilon}_B) A_o \tag{4}$$

In which dynamically-enhanced stress function  $\sigma^*(\hat{\varepsilon}_B)$  in Eq. 4 can be expressed as:

$$\sigma^*(\hat{\varepsilon}_B) = N_1 \sigma_y + N_2 K(\hat{\varepsilon}_B)^n \quad \to \quad \sigma_y + K(\hat{\varepsilon}_B)^n \quad \text{ for } \quad N_1 = N_2 = 1$$
 (5)

 $M_o$  refers to the mass of impactor,  $A_o$  refers to the cross-sectional area of cellular material and x(t) is the position of shock wave front at time, t. Note that x(t) does not represents the Lagrangian position of the shock wave front since the particle velocity in the pre-shock region is non-zero. Combining Equation (3) and (4) to obtain expression of x(t), the relative velocity of shock wave front can be obtained by taking its time derivative. The  $m = \frac{M_o}{A_o}$  refers to the specific mass.

$$\frac{d}{dt}x(t) = -\frac{mk(\hat{\varepsilon}_B)}{\rho_o \sigma^*(\hat{\varepsilon}_B)} \exp\left(-\int_{\hat{\varepsilon}_o}^{\hat{\varepsilon}_B(t)} \frac{k(\hat{\varepsilon}_B)}{\sigma^*(\hat{\varepsilon}_B)} d\hat{\varepsilon}_B\right) \frac{d\hat{\varepsilon}_B}{dt}$$
(6)

By combining with the relative shock speed  $(\dot{x})$  illustrated in Figure 3-5 and performing integration, the time function with respect to the development of shock strain and stress directly behind the shock wave front can be expressed as follows.

$$t = -T \int_{\hat{\varepsilon}_o}^{\hat{\varepsilon}_B(t)} \frac{f^*(\hat{\varepsilon}_B) \sqrt{\sigma_y \hat{\varepsilon}_B}}{\sqrt{\alpha \hat{\varepsilon}_o (\sigma(\hat{\varepsilon}_B) - \sigma_y)}} d\hat{\varepsilon}_B$$
(7)

 $f^*(\hat{\varepsilon}_B)$  is a dimensionless function, T is the characteristic time parameter,  $\alpha$  is the stress-enhancement parameter and  $\hat{\varepsilon}_o$  refers to the initial plastic shock strain. See **Annex B** for the definitions of the respective parameters. The characteristic parameter T generally relates the time when the initial kinetic energy of mass is converted into internal energy (i.e. depending on the elastic yield stress) within the cellular material.

With the incorporation of the dynamically-enhanced stress function (i.e. Eq. 5) and solving all integrals, the final expression for the time function with respect to shock strain is as follows.

$$t = T \left( 1 - \left( \frac{\alpha}{\left( \frac{\hat{\mathcal{E}}_B}{\hat{\mathcal{E}}_O} \right)^{-n} + \alpha} \right)^q \right)$$
 (8)

Re-arranging the above expression will give us shock strain function in time domain. It is imperative to note that  $\hat{\varepsilon}_B$  does not refer to the actual strain value, but to the plastic shock strain. The actual strain value can be evaluated by evaluating  $\varepsilon_B = \hat{\varepsilon}_B + \varepsilon_Y$ .

$$\hat{\varepsilon}_B = \hat{\varepsilon}_B(t) = \hat{\varepsilon}_o \left( \frac{1 + \alpha}{\left(1 - \frac{t}{T}\right)^{\frac{1}{q}}} - \alpha \right)^{-\frac{1}{n}}$$

$$(9)$$

Given that  $\sigma(\hat{\epsilon}_B) = \sigma_y + K(\hat{\epsilon}_B)^n$ , the function to describe the time-dependent dynamically-enhanced material stress is:

$$\sigma(\hat{\varepsilon}_B) = \sigma_B(t) = \sigma_y \left( 1 + \alpha \left( \frac{1 + \alpha}{\left( 1 - \frac{t}{T} \right)^{\frac{1}{q}}} - \alpha \right)^{-1} \right)$$
(10)

The velocity-time function that describes motion of debris and crushed material, relative to the particle velocity for material within the pre-shock region can also be obtained with the following relationship:

$$v_{Brelative} = \left(V_o - v_{A_{initial}}\right) \left(\frac{1+\alpha}{\left(1-\frac{t}{T}\right)^{\frac{1}{q}}} - \alpha\right)^{-q} \tag{11}$$

Using the mass and momentum conservation across the shock wave front as the base equations, the plastic shock wave velocity relative to the particle velocity in the pre-shock region can be evaluated as follows.

$$\dot{x} = \frac{V_o - v_{A_{initial}}}{\hat{\varepsilon}_o} \left( \frac{1 + \alpha}{\left(1 - \frac{t}{T}\right)^{\frac{1}{q}}} - \alpha \right)^{q - 1}$$
(12)

In summary, the following calculation procedures are performed during the analytical model predictions:

- Establish the power-law parameters (i.e. strength index K and strain hardening index n) that describe the strain densification regime of the foam material
- Compute initial plastic shock strain  $\hat{\varepsilon}_B$ , stress enhancement parameter  $\alpha$ , characteristic time parameter T
- Evaluate plastic shock strain-time function  $\hat{\varepsilon}_{R}$  (See Equation 9)
- Evaluate shock stress-time function  $\sigma(\hat{\epsilon}_B)$  (See Equation 10) to give shock-induced stresses behind the shock wave front
- Evaluate velocity-time function that describes the motion of debris and crushed material behind the shock wave front. This absolute velocity-time curve can be determined by adding  $v_{A_{initial}}$  to the relative velocity-time function (Equation 11). In this respect, it is assumed that the  $v_{A_{initial}}$  remains constant over time

- Determine debris penetration distance by finding the area under the velocity(absolute)-time curve
- Similar approach is used to determine the shock wave termination distance.

## 3.3. Inputs to Analytical Model Predictions

A single debris penetration problem is examined with both R-PLH Model and Modified-R-PLH Model. A specific impact mass of 375 kg/m<sup>2</sup> is considered for the concrete debris with thickness of 0.15 m and density of 2500 kg/m<sup>3</sup>. From the empirical stress-strain curve of the foam R110WF obtained from Arezoo in [2], the power-law parameters (i.e. strength index K and strain hardening index n) that describe the strain densification regime have been determined. Together with the foam material properties listed in Table 2-1, the time-function of shock strain and stress, relative debris and shock wave velocity are computed.

#### 3.4. Results/Discussions

Figure 3-6 compares the development of shock-induced strains and stresses closely behind the wave front for both analytical models, under the debris launch velocity of 145 m/s. The Modified R-PLH Model predicts lower shock strains and stresses. This phenomenon seems rational; with the inclusion of elastic yield strain and non-zero particle velocity for materials in uncrushed region, the effects (i.e. magnitudes of shock stress and strain) coming from the debris impact are likely to be attenuated, as compared to a more "rigid" material (i.e. R-PLH Model). As the plastic wave weakens over time, it is reasonable to see that the shock stress decreases towards yielding stress. It is expected as well that the shock strain shall reduce to yield strain. However, due to truncation errors in both analytical models, the lowest shock strain computed is still higher than the yield strain of 0.0286. However, these errors are insignificant to affect the overall debris penetration results and can be ignored.

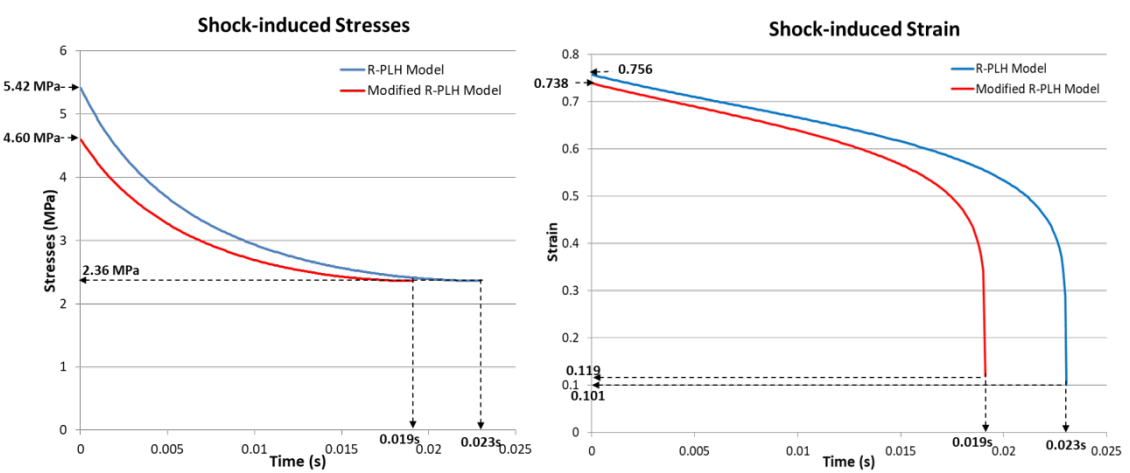


Figure 3-6: Comparison of shock strains and stresses-time history plots from analytical models, under debris launch velocity of 145m/s

The debris and shock wave velocity-time curves for both models are illustrated in Figure 3-7. Modified-R-PLH Model predicts a slower rate of velocity decrease for both the debris and plastic shock wave, as compared to R-PLH Model. It is worth to mention two specific assumptions made in the Modified-R-PLH Model; (1) particle velocity  $v_{A_{initial}} = 24.77 \, m/s$  due to elastic wave remains constant during entire penetration process and that (2) this particle velocity drops instantaneously to zero at the time of shock wave termination, i.e. when the shock wave velocity equals the particle velocity in the elastic precursor.

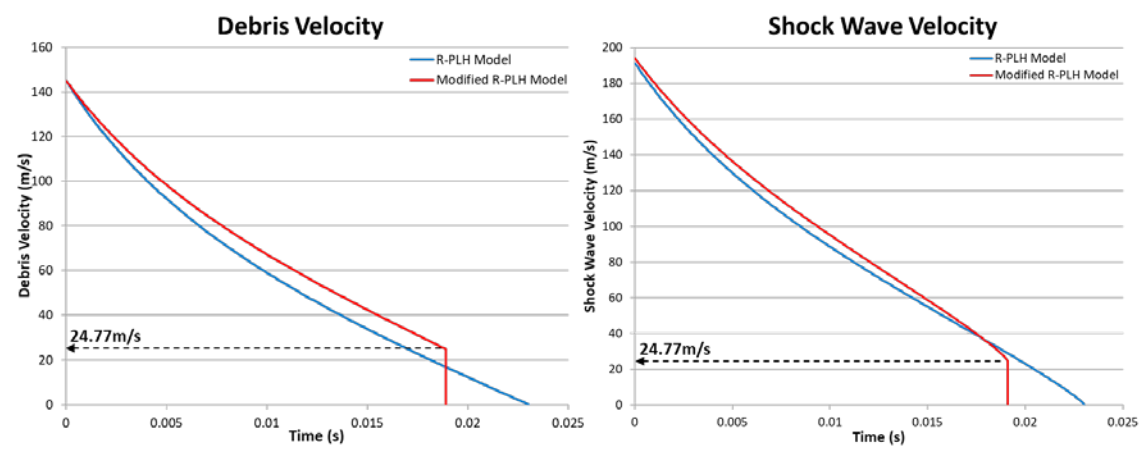


Figure 3-7: Comparison of debris and shock wave velocity-time curves from analytical models, under debris launch velocity of 145m/s

Both debris penetration distance and shock wave termination distance can be easily computed by finding the area under the curves. Table 3-2 consolidates the analytical results for cases with different debris launch velocities.

Table 3-2: Summary of results from analytical models predictions

	50 m/s		100 m/s		145 m/s	
Model Parameters	R-PLH	Modified R-PLH	R-PLH	Modified R-PLH	R-PLH	Modified R-PLH
Initial Shock Stress (MPa)	2.783	2.484	3.893	3.299	5.417	4.600
Initial Shock Strain	0.651	0.564	0.718	0.662	0.757	0.738
Debris penetration distance (m)	0.190	0.149	0.692	0.707	1.316	1.424
Shock wave termination distance (m)	0.316	0.195	1.054	0.972	1.922	1.951

## Preliminary Design of Soft-catcher (based on Modified R-PLH Model's Predictions)

From these analytical results, it is apparent to establish a preliminary design length of 2 m for the soft-catcher, based on the shock wave termination distance computed with debris launch velocity of 145 m/s. The shock wave termination distance essentially consists of the debris penetration distance and the material crushing length ahead of the debris. The impact stresses acting on the debris are evaluated based on the initial shock stress at time t=0. The highest initial shock stress of 4.6 MPa is observed for the case when debris launch velocity is 145 m/s. This shock stress is about 13.1% of concrete compressive strength, considering the design strength of 35 MPa. As one prerequisite to ensure no additional damage to debris during soft-catching process, the maximum induced shock stress shall preferably be less than say 20% of the concrete compressive strength.

Some of the important assumptions made in the analytical models include the following:

- Single rigid debris penetration
- Infinite thickness of soft-catcher
- Same velocity for debris and the crushed particle in plastic zone
- Uniform shock-induced stress distribution behind shock wave front (i.e. within crushed zone)
- Material reach yielding stress and strain when elastic wave passes through

- Material subjected to constant (i.e. in time domain) particle velocity  $v_{A_{initial}}$  when elastic wave passes through

In which, the validity and consequences of these assumptions are verified through numerical analyses. **Annex C** gives a comprehensive list of model assumptions.

## 4. Feasibility Study and Design (Stage 2A) – 1-D Numerical Predictions

Numerical analyses are performed using LS-DYNA FE simulation code, while the pre and post-processing of the models are carried out by LS-PrePost. The soft-catcher is modelled using MAT\_63 (CRUSHABLE FOAM). Cubic elements, subjected to compressive and tensile loading tests, are first performed to verify the quasi-static and dynamic constitutive responses of this selected material model. This material model generally represents an isotropic crushable foam material that responds mainly in one-dimensional manner. The compressive tests with different applied loading rates (See Figure 4-1) has showed that this material model exhibits strain rate-sensitive behaviour (i.e. stress increases with higher loading rates). At this juncture, it is worth to highlight that the elastic limit strains obtained from the numerical models, even for the case with lowest loading rate of 0.001 m/s, are apparently higher (i.e. about 0.034) than the prescribed elastic strain value of 0.0286. The elastic limit strain for models with loading rates higher than LR10 (i.e. LR10 refers to loading rate of 10 m/s) is approximately 0.0343.

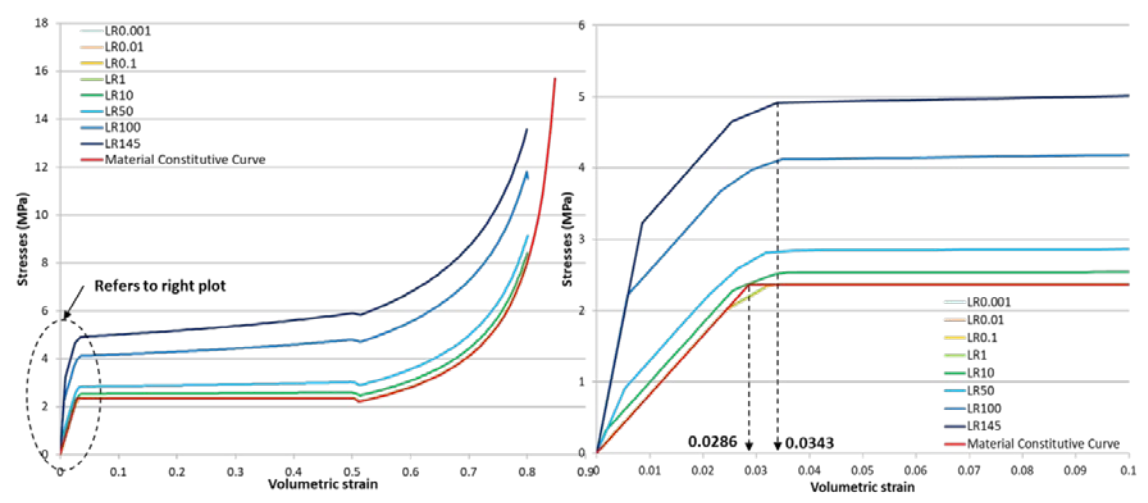


Figure 4-1: (Left plot) – Stress vs volumetric strain plots for models with different loading rate (m/s)

On the other hand, the concrete debris is modelled using MAT\_20 (RIGID). See **Annex D** for more information pertaining to the setup of the numerical models for material model validation and the 1-D FEM analyses (e.g. element formulation, hourglass control, contact algorithm, timestep control etc.).

In the first part of this section, 1-D numerical models are constructed with target length of 20m, in order to eliminate the influence of end boundary to the shock wave propagation during debris deceleration time. These numerical results are compared against the analytical model prediction presented in Section 3.4, in the interest of verifying various assumptions made in the analytical models (See **Annex C**). The second part of this section evaluates the end boundary effects on the soft-catcher's responses, using target length of 2m. The resultant numerical predictions of design outputs (i.e. penetration distances, initial shock stresses and

strains etc.) for the soft-catcher are presented to highlight the consequences of simplification in analytical model predictions.

## 4.1. Results and Discussions for Verification of 1-D Analytical Models

In this verification exercise, mesh sensitivity study is performed with element sizes of 0.050m, 0.025m and 0.010m, to examine the mesh density effect. It is observed that results (i.e. shock stresses, strains and plastic wave termination distance) from numerical model with finer mesh size correlate better with Modified-R-PLH Model. Further studies with more refined mesh sizes (e.g. 0.005m, 0.0025m and 0.001m) have shown that numerical results are converged when mesh sizes used are smaller than 0.010m. In this respect, the following numerical results presented are obtained from models with element size of 0.010m.

#### **Material Stress**

The left plot of Figure 4-2 shows the compressive stress-time histories for Element 5, 50 and 100 in the numerical model to closely examine on the development of material stresses over time. These elements are located at 0.05m, 0.5m and 1.0m from the impact end of target respectively. In this plot, the shock stress-time function from Modified-R-PLH Model is included for the purpose of comparison. The "first" peak stresses for these elements can be visibly identified, which appears to correlate relatively well with the analytical predictions. These initial peak stresses, which decrease with time, are induced when the plastic wave front propagates through these elements. It can be evidently seen that prior the arrival of shock wave front, Element 50 and 100 experience an initial build-up of stresses up to yielding stress level. This phenomenon is primarily attributed by the presence of precursor elastic wave. This is not as obvious for Element 5 since the separation distance between the plastic and elastic waves are generally small during the early phase of impact duration. Furthermore, it can be ascertain that the general assumption of uniform material stresses across spatial domain within the crushed zone (i.e. post-shock region) is invalid, especially when the shock wave propagates further away from the impact end. In fact, these shock-induced stresses appear to decrease towards the impact end, with the highest stress located at the wave front. This also implies that the numerical model predicts lower resultant shock stresses within the plastic zone, as compared to the analytical model. In fact, this observation of lower resultant shock stresses in the numerical model agrees well with the velocity-time curves of the impactor. The right plot of Figure 4-5 shows that velocity difference (i.e. velocity of impactor in the numerical model minus velocity of impactor in the analytical model) is increasing over time. The lowering of shock stresses in numerical model results in slower deceleration of the impactor.

The right plot of Figure 4-2 presents the "first" peak stresses of target elements, in models of different impact velocities, up to 2m from the impact end of target, in comparison with the analytical model predictions. It is established that the predictions from Modified-R-PLH Model fit relatively well with the numerical results. With the increases of time, these "first" peak stresses of the elements generally reduce towards yielding stress value of 2.36MPa. This is expected since the reduction of shock-induced stresses shall follow the stress reduction path of the material's constitutive curve (See Figure 3-4). It is good to mention that as these peak stresses reach the yielding stress value, it also signifies the cessation of the plastic shock wave propagation.

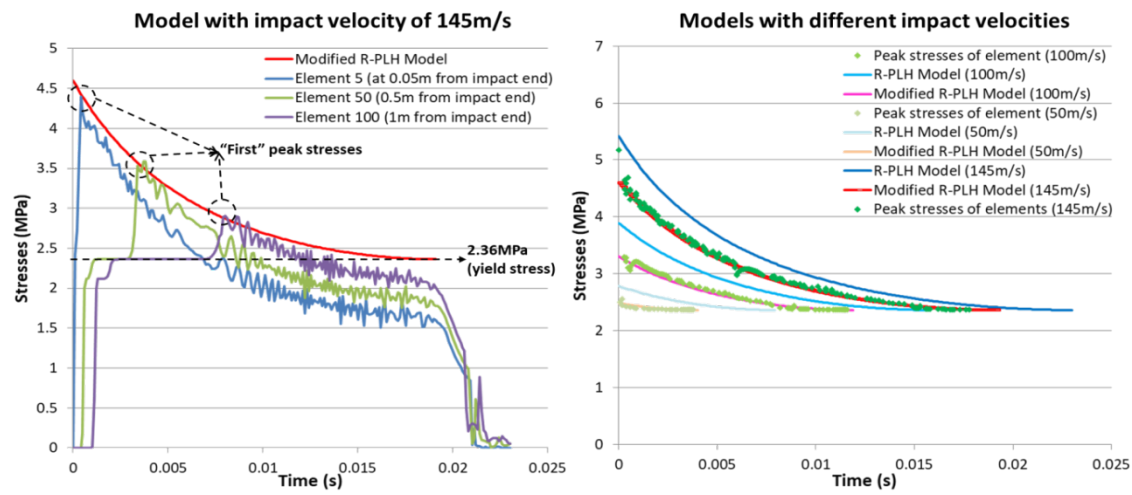


Figure 4-2: (Left plot) – Comparison of stress-time history curves of selected target elements with Modified-R-PLH Model predictions. (Right plot) – Comparison of peak stresses of target elements (up to 2m from impact end) in models of different impact velocities, with R-PLH Model and Modified-R-PLH Model

#### Material Strain

Figure 4-3 presents the volumetric strain-time histories of selected elements for model with impact velocity of 145m/s, in comparison with Modified-R-PLH Model. Due to presence of precursor elastic wave, elements are first induced to elastic strain, before plastic wave front further increases the strain to peak shock strain levels. It is illustrated that these initial shock strains for successive elements generally reduce over time, till it reach the yield strain level (i.e. similar explanation can be given with the reduction of shock-induced stress and strain along the material's constitutive curve). The pre-defined elastic yield strain value for the foam material is 0.0286 (See Table 2-1). However, the elastic strain limit obtained from the numerical analysis is approximately 0.0343. This difference is observed in the validation of material model MAT\_63 under compressive loading tests, as discussed earlier.

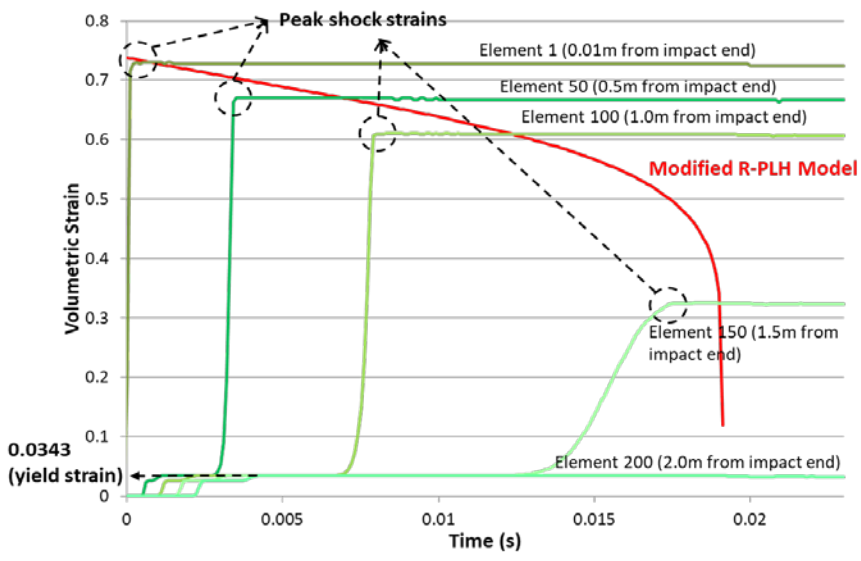


Figure 4-3: Comparison of volumetric strain-time history curves of selected target elements with Modified-R-PLH Model, with impact velocity of 145m/s

In comparison with Figure 4-3, Figure 4-4 shows that as the debris impact velocities decreases, the time taken for the 1<sup>st</sup> element to reach its maximum volumetric strain increases. This phenomenon deviates from the analytical model predictions, as the analytical models

"ideally" assume that initial shock strain will be induced at time t=0. Nevertheless, Modified R-PLH Model appears to provide better correlation with the numerical results. However, it is noted that the predictions of higher shock strain from the analytical models appear to relate well with the phenomena observed from the validation exercise for the material model (MAT\_63) (See Figure 4-1). For a given stress value, the dynamic constitutive curve under a higher loading rate gives a lower corresponding volumetric strain, as compared to the material's quasi-static constitutive curve. At this juncture, it is good to highlight that the analytical model predictions are formulated using the material's quasi-static constitutive relationship.

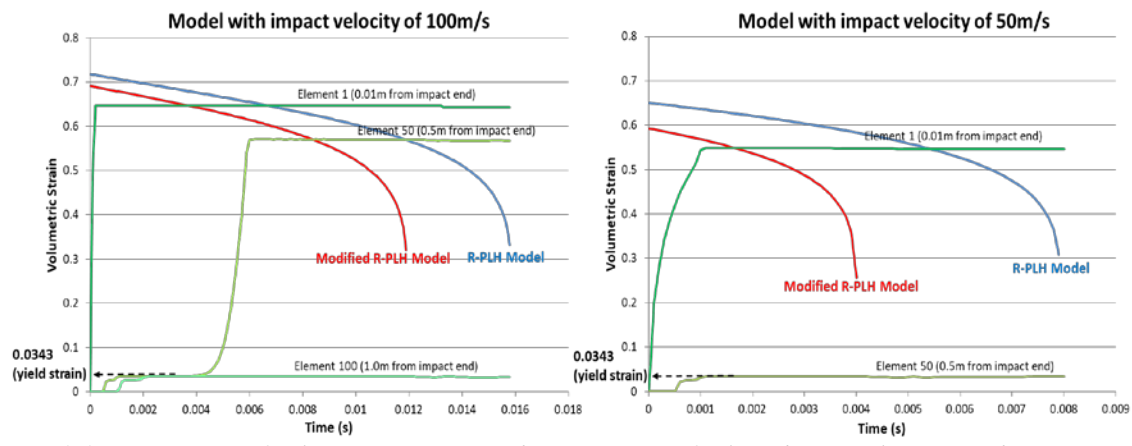


Figure 4-4: Comparison of volumetric strain-time history curves of selected target elements with R-PLH Model and Modified-R-PLH Model, with impact velocities of 50m/s and 100m/s

#### Particle and Debris Velocity

In both R-PLH Model and Modified-R-PLH Model, it is assumed that the shock stress (closely behind the plastic wave front) is the component that resists the motion of the impactor and the crushed material behind the wave front (See Eq. 4). This implies that both the impactor and the crushed material are presumed to travel at the same velocity during the penetration process. Indeed, the left plot of Figure 4-5 verifies this phenomenon. Velocity-time curves of selected elements located at 0.1 m, 0.5 m, 1.0 m and 2.0 m respectively from the impact end are plotted against the impactor's velocity-time curve. It can be seen that an initial velocity of approximately 26.57 m/s is induced on the elements due to the presence of precursor elastic wave. This initial particle velocity remains constant over time, until subsequently when the shock wave arrives, this particle velocity increases to match with the impactor's velocity. Hence, this observation verifies the Modified-R-PLH Model's assumption on the constant initial particle velocity due to precursor elastic waves. Note the difference in the elastic velocity of 26.57 m/s, as compared to analytical prediction of 24.77 m/s which is computed using Eq.(1). This could be attributed by the steeper slope of stress-strain curves in numerical models with higher loading rates (See Figure 4-1).

The right plot of Figure 4-5 shows that the velocity-time curve predicted by Modified-R-PLH Model is relatively in good agreement with the numerical model, even though slight differences can be observed as time increases (See earlier discussion on shock-induced stresses within the crushed zone). Nevertheless, this consistency between the Modified-R-PLH Model and numerical model is observed only from time t=0 to time in which debris velocity reaches near the initial particle velocity of 24.77 m/s. This is because Modified-R-PLH Model provides predictions of material responses during the plastic wave propagation. When the termination time is reached (i.e. shock stress reaches elastic yielding stress), this

model assumes that the initial particle velocity (i.e. due to elastic wave) drops instantaneously to zero. However, this model assumption appears to be invalid, as observed from the numerical model. As the impactor's velocity goes below the initial particle velocity (i.e. due to elastic waves), the impactor continues to move at a slower deceleration rate as before.

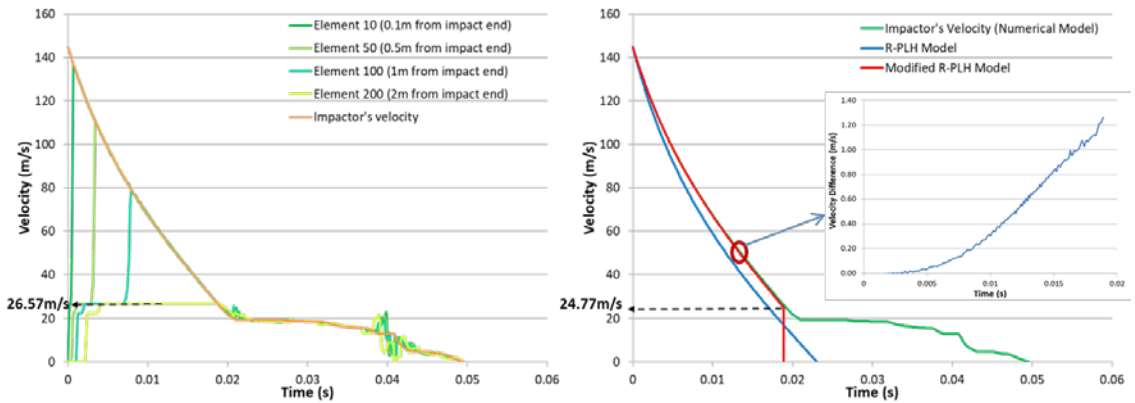


Figure 4-5: (Left plot) - Velocities of selected elements in comparison with impactor's velocity for numerical model with impact velocity of 145m/s (Right plot) – Velocity-time history of impactor (numerical models) in comparison with R-PLH Model and Modified R-PLH Model, with impact velocity of 145m/s

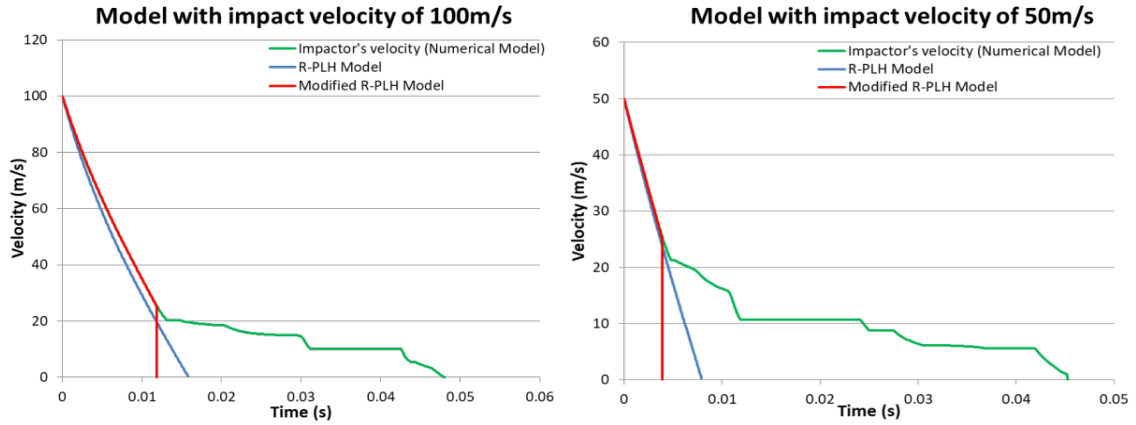


Figure 4-6: Velocity-time histories of impactors in numerical models of impact velocities of 50m/s and 100m/s

Transition between two distinct impactor's velocity time response regimes can be clearly identified from the numerical models shown in Figure 4-5 and Figure 4-6. These regimes appear to associate with target responses under different stages of wave propagation. During the initial impact phase (i.e. termed as higher velocity response regime), both plastic and elastic wave propagation are relevant. Energies from the moving mass are largely dissipated through material crushing during shock wave propagation, which resulted in steady deceleration of impactor. It is also established that in all the numerical models, shock waves terminate (i.e. the shock stresses and strains of target elements reach yielding level) at times near the interface of these two response regimes. This implies that only elastic stress waves are propagating in the later part of impact process (i.e. termed as lower velocity response regime). This also further explains the presence of horizontal velocity plateaus, during which minimal or no losses of impactor energies. In fact, the overall travelling distances of impactor will increase as the target length increases. Therefore, with these findings in mind, it brings out the need to evaluate the responses of numerical models with a target length that is equivalent to the soft-catcher's design, in order to establish more reliable predictions of the soft-catcher's responses.

## 4.2. Results and Discussions for Effects of Rigid Backing

The previous section has demonstrated that the Modified R-PLH Model, with the accounts of changes in material states due to induced elastic stress wave, agrees relatively well with the numerical model predictions, in particular during the higher velocity response regime. The preliminary design of soft-catcher (see Section 3.4) formulated using analytical approach (i.e. Modified-R-PLH Model) only effectively "accounts" for the soft-catcher responses during the time when plastic shock wave is still propagating. However, the presence of finite thickness of soft-catcher will have influences on how the soft-catcher responds, in particular during the lower velocity response regime, which ultimately depends on the overall length of target. Hence, this section examines numerical results from models with 2 m target length (2mTL) and element size of 0.010 m.

The left plot of Figure 4-7 compares the "first" peak stresses of elements (within 1.3 m from impact end) of 2mTL model with Modified-R-PLH Model, as well as comparing the respective stress-time history curves of selected elements in the 2mTL and 20mTL model. The right plot of Figure 4-7 compares the "first" peak stresses of elements in 2mTL model, under lower impact velocities of 50 m/s and 100 m/s, with analytical model predictions. For the models with lower impact velocities (i.e. 50 m/s and 100 m/s), consistencies in predicting the shock-induced stresses are again observed between the Modified-R-PLH Model and the 2mTL numerical models during the higher velocity response regime. However, in the model with impact velocity of 145m/s, target elements experiences surges in stresses during the later part of the higher velocity response regime (i.e. before the reduction of shock stresses reaches yielding level). This is primarily influenced by the end boundary located at 2 m from impact end. This observation also signifies that the time in which the shock wave terminates cannot be easily identified from various material responses (i.e. stress-time history, velocity-time curves of impactor).

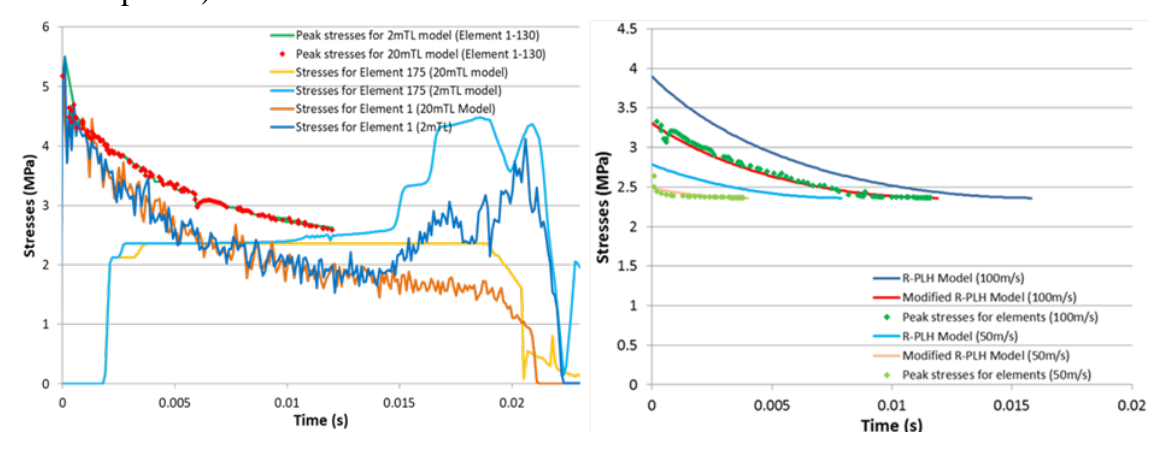


Figure 4-7: (Left plot) – Comparison of "first" peak stresses of elements (within 1.3m from impact end) of 2mTL model with analytical model predictions, as well as stresses of selected elements in 2mTL and 20mTL model. (Right plot) – Comparison of "first" peak stresses of elements in 2mTL, under lower impact velocities, with analytical model predictions.

In view of evaluating the impact stresses experience by the impactor (i.e. debris), it is worth to examine the stress-time history of Element 1 (i.e. element located at the front of target) of 2mTL model, under impact velocity of 145 m/s. Figure 4-7 shows that even with the influence end boundary at 2 m, the "first" peak stress of Element 1 is the highest stress level for the entire penetration duration.

Figure 4-8 compares the velocity-time curves of the 2mTL models under different impact velocities, with the predictions from Modified R-PLH Model. The velocity rate of impactor in the 2mTL model, under impact velocity of 145 m/s, is observed to deviate from the 20mTL model at time even before reaching near the interface between the higher and lower velocity time response regimes. This further substantiates the earlier hypothesis that the shock wave propagation in the 2mTL model with impact velocity of 145 m/s is affected by the end boundary condition.

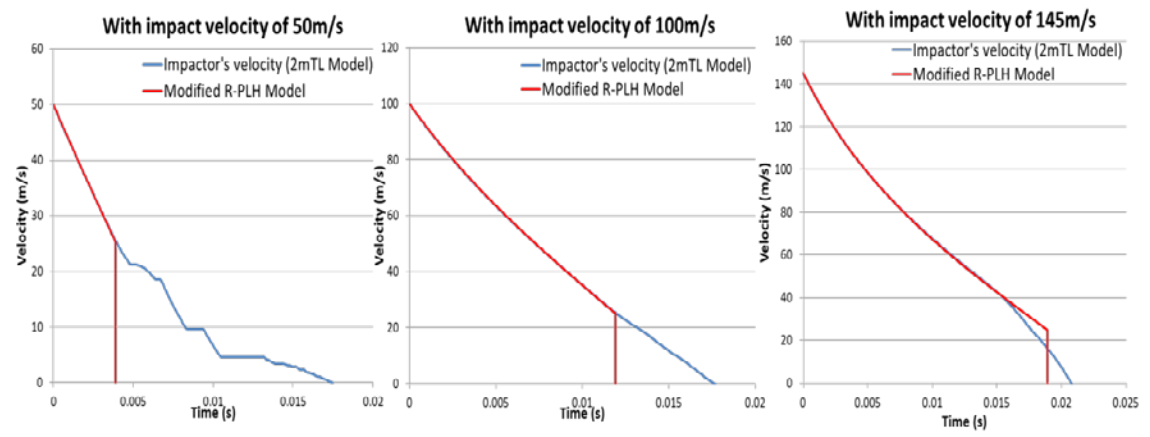


Figure 4-8: Comparison of velocity-time curves for 2mTL models under different impact velocities, with Modified R-PLH Model

The end boundary support reaction can be extracted from the numerical model. Figure 4-9 illustrates the reaction forces in the impact direction (i.e. X-direction) for models with different impact velocities. The onset of initial peak reaction forces of about 0.23 kN in the negative-X direction occurs at time that corresponds to the induced elastic stress wave reaching the end of the soft-catcher (i.e. about 0.0023 s for a linear sound speed (866 m/s) of stress wave to travel a distance of 2 m). Given the elastic yielding stress of 2.36 MPa for the foam material, the total amount of force (in positive X-direction) exerted by the elastic wave onto the end boundary of this 2D model can be analytically computed as 0.236 kN, considering a surface area at end boundary of  $10^{-4}$  m<sup>2</sup> (i.e. for element size of 0.010 m). The subsequent increase in reaction forces (i.e. up to about 0.45 kN) for model with impact velocity of 145 m/s are primarily attributed by shock wave.

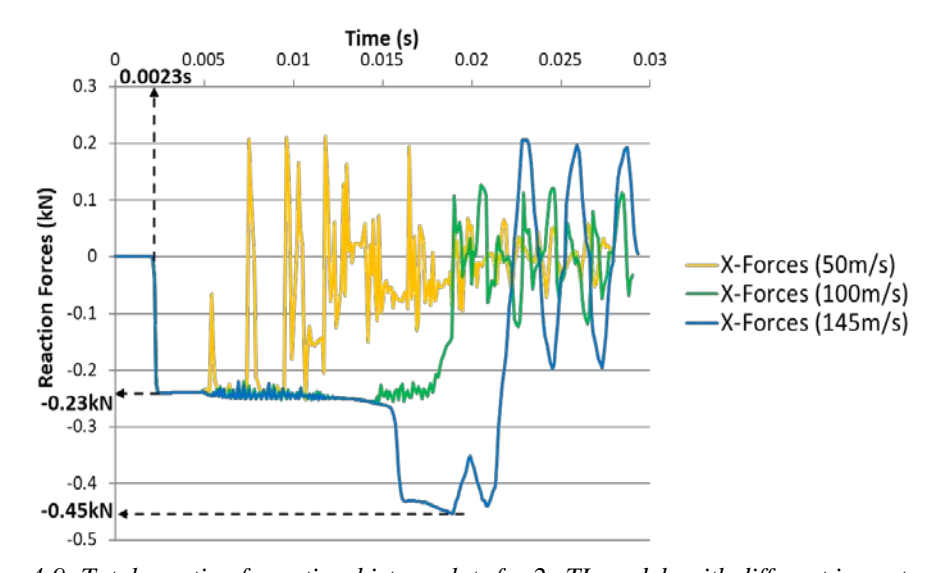


Figure 4-9: Total reaction force-time history plots for 2mTL models with different impact velocities

## Consequences to Design of Soft-catcher - Simplifications in Modified-R-PLH Model

It is apparent to see that with the inclusion of elastic strain (i.e. for material ahead of shock wave front) and constant initial particle velocity due to elastic waves, Modified-R-PLH Model improves the correlations of shock stresses and strains with the numerical results, as compared to R-PLH Model. This gives good explanation on the consistencies in impactor's velocity-time curves observed within the higher velocity time response regimes, for all cases with three different impact velocities. However, as the Modified-R-PLH Model simplifies the approach by assuming an abrupt termination of the constant initial particle velocity once the shock stresses and strains reach yielding level (i.e. termination of shock wave front), the analytical results deviate in predicting the overall debris penetration distance. In fact, it can be seen that this deviation becomes more significant as the debris launch velocity decreases. Nevertheless, the deviation in debris penetration distances for the scenario with design impact velocity of 145m/s is negligible (i.e. 0.004m) and hence, the preliminary design length of soft-catcher remains valid.

Even though the predictions of shock stresses by Modified-R-PLH Model agree relatively well with the numerical models, the "first" peak stresses of Element 1 in numerical models are higher than the initial shock stress (i.e. at time t=0) from Modified-R-PLH Model. Furthermore, Modified-R-PLH Model cannot predict any surges in material stresses due to presence of end boundary, since analytical model assumes infinite thickness of target. Considering these differences, it is recommended that the impact stresses acting on the debris shall be considered based on the numerical predictions.

Table 4-1 consolidates and compares the design outcomes from Modified-R-PLH Model and the 2mTL numerical models, for different debris launch velocities.

Table 4-1: Summary of results from 2m1L numerical model and Modified R-PLH Model								
	50m/s		100m/s		145m/s			
Model Parameters	Modified	2mTL	Modified	2mTL	Modified	2mTL		
	R-PLH	Model	R-PLH	Model	R-PLH	Model		
Initial Shock Stress (MPa)	2.484	2.637	3.299	3.326	4.600	5.504		
Debris penetration distance (m)	0.149	0.270	0.707	0.780	1.424	1.420		
Max End Boundary Reaction Force in negative-X direction (kN)	-	0.23	-	0.255	-	0.453		

Table 4-1: Summary of results from 2mTL numerical model and Modified R-PLH Model

#### 5. Feasibility Study and Design (Stage 2B) – 2-D Numerical Model Predictions

Section 2.1 has earlier identified the intention to catch the wall debris at close distance so that penetration problem deals only with single large wall debris moving at its initial launch velocity. Previously, the approach to dissipate debris motion energies through one-dimensional compressive crushing of soft-catcher material are examined and discussed. Now, efforts are focused on studying how these design parameters can be influenced through material tensile and shear stress failure within the soft-catcher. In this context, stress waves will propagate in two-dimensional (2-D) space domain. The support reaction forces induced at boundary ends and the material stresses within the soft-catcher are presented and compared with corresponding observations in 1-D models. Figure 5-1 presents the top and front view of wall debris-soft catcher impact scenario.

Figure 5-2 shows the 2-D numerical model, with an overall length of 2 m and a height of 1.25 m. The thickness of both the wall debris and soft-catcher are defined by the element size of 0.010 m in the y-direction. The lateral and end boundary supports restrain translational movements in all directions, while the bottom edge only allows translational displacement in X-direction. Rotational motions are released in all directions.

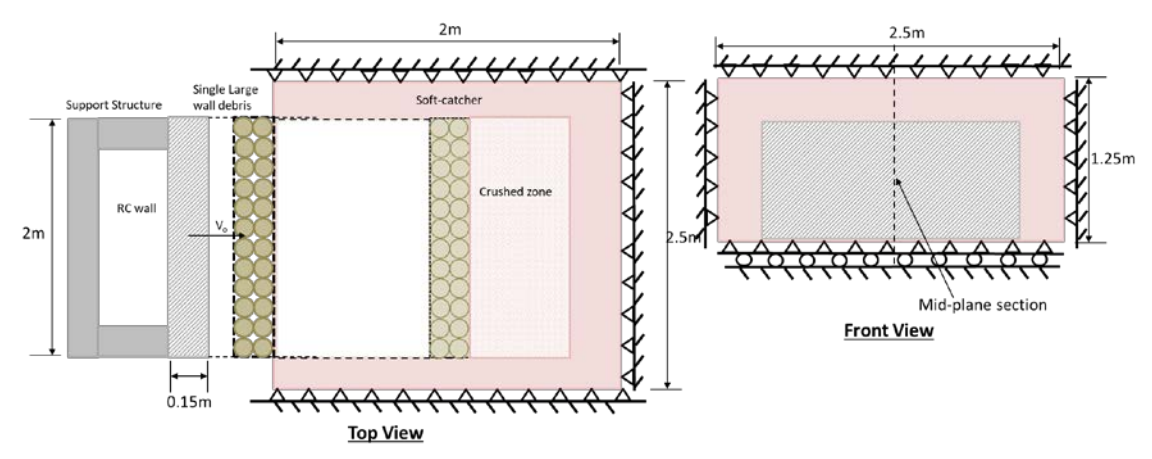


Figure 5-1: Top and front view of wall debris-soft catcher impact scenario

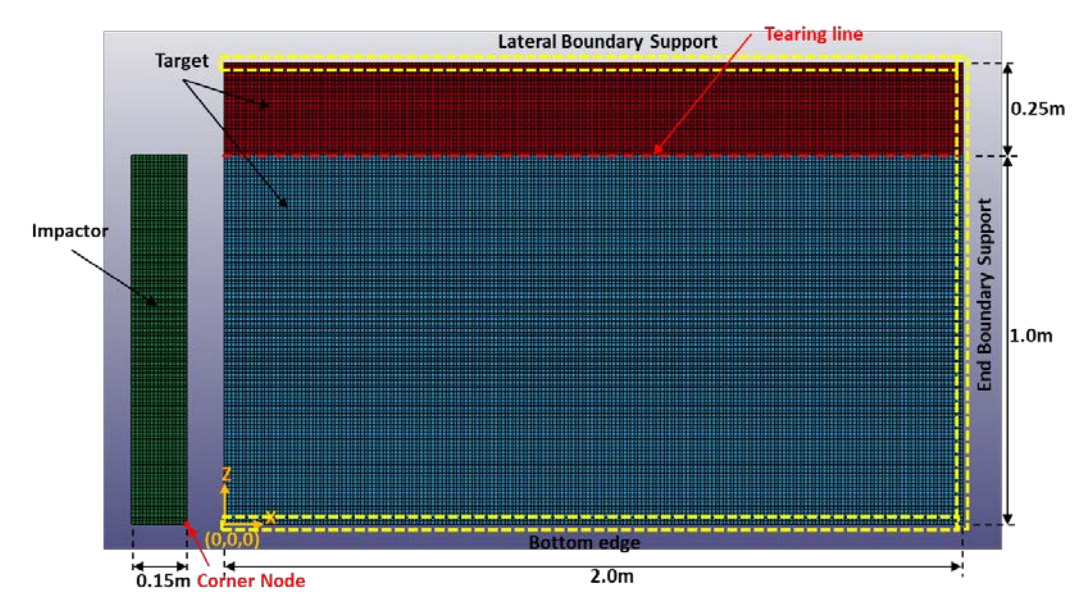


Figure 5-2: 2-D numerical model

In this 2D numerical modelling, a horizontal tearing line, governed by a stipulated stress-based material failure criterion, is pre-defined as shown in Figure 5-2. An additional contact interface algorithm known as CONTACT-AUTO-SURFACE-TO-SURFACE-TIEBREAK in LS-DYNA is introduced into the analyses to account for the tensile and shear resistances within the soft-catcher along this tearing line. The shear and tensile failure stress of 2.17 MPa and 1.86 MPa are incorporated respectively, according to Table 2-1. The approach of using tiebreak contact to establish a tearing line largely simplifies the modelling of failure mechanism within the soft-catcher. Realistically, crushing of foam material can also occur within the overlying foam material above the tearing line, as the wall debris cloud expands further. A common approach to account for continuum-based material failure is by the use of element erosion technique, which will give a more realistic material response of the soft-catcher. However, this erosion technique is avoided in our modelling approach as it carries

higher risk of numerical inaccuracies especially when severe deformations of elements in soft material are expected. Furthermore, premature terminations of analyses can occur due to negative volumes of highly distorted elements. Nevertheless, considering that the crushing failure of foam material predominately localised within the impact region (i.e. below the tearing line), it is reasonable to assume tearing line failure.

## 5.1. Results and Discussions for 2-D Numerical Analyses

#### **Debris Velocity**

The debris velocity-time history plots for the 2-D model under various impact velocities are compared against both the 1D numerical and analytical model, as shown in Figure 5-3. During the initial phase of impact duration, the decelerations of debris in the 2D models relate fairly well with the 1D model predictions. For the 2-D models with lower impact velocities of 50 m/s and 100 m/s, debris decelerations appear to slow down towards the later phase of the impact process. Possible reason to support this observation include: in the 2-D model, vertical stress waves are likely to weaken the horizontal stress waves that oppose the debris motion. Unlike in 1-D model, stress waves are allowed to propagate only along the impact direction. Furthermore, with the opening created along the tearing interface as the material fails in the 2-D model, the nodes within the soft-catcher are allowed to translate vertically. With multiple elastic waves reflection in the 2D space domain, losses in contact between debris and frontal face of soft-catcher can occur and result in further reduction of compressive stresses (i.e. in the X-direction) within the soft-catcher that resist the debris motion. However, it is apparent to see that the differences between velocity-time curves of these models reduce as the initial impact velocity of debris increases. The 2D model with higher impact velocity of 145 m/s shows a rather similar deceleration profile with the 1D numerical model.

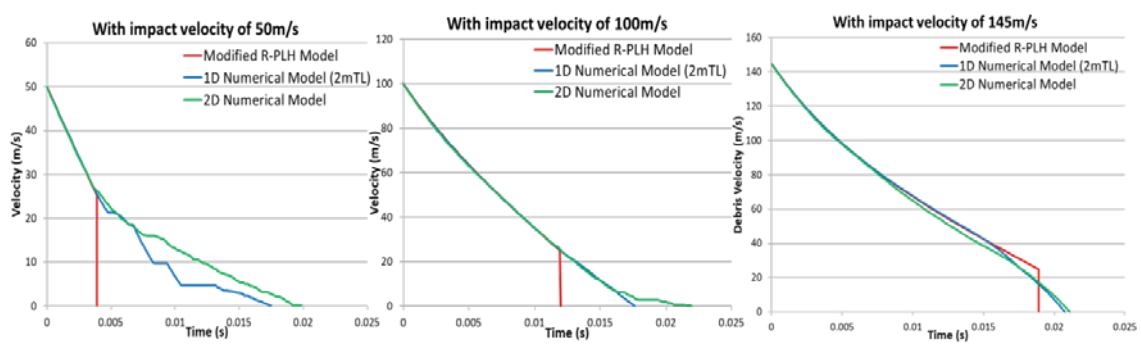


Figure 5-3: Comparison of velocity-time curves of impactors in 2D, 1D numerical and analytical model

#### Impact Stresses on Debris

To establish the link between deceleration of debris and the compressive stress-time histories of elements located over the frontal face of the soft-catcher, Figure 5-4 compares the averaged compressive-stress time histories of all front elements in model with impact velocity of 100 m/s, with the stresses of Element 1 in 1-D numerical model. It is found that these elements in 2-D Model experience larger stress oscillations during the debris penetration process, as compared with the 1-D model. This consequently results in less momentum transfers from the debris, which motivates further decreases in debris deceleration for the 2-D model. Note that the time of occurrence for these stress oscillations in 2-D model coincides well with the time in which the debris velocity-time curve in 2-D model deviates from the 1-D curves (See Figure 5-3). There are few possible reasons that can explain the occurrence of stress

oscillations observed in the 2D Model. These include sudden losses of connectivity of nodes along the tearing interface due to material failure, or losses of contact at front interface between debris and soft-catcher.

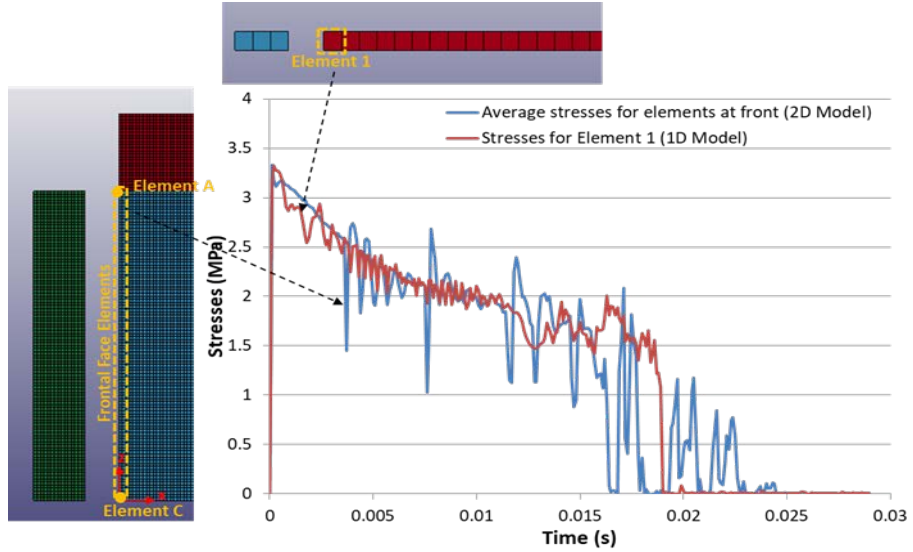


Figure 5-4: Compressive stresses-time histories of front elements in 2D and 1D Model (with impact velocity of 100m/s)

In order to evaluate the maximum impact stresses acting on the debris, Figure 5-5 illustrates the compressive stress-time histories plots of Element A and C (See Figure 5-4) along the frontal face of the soft-catcher in 2-D model, against the Element 1 in 1-D numerical model, under various impact velocities. The 1-D model predicts initial impact stresses (i.e. at time t=0) lower than the one obtained from the 2-D model. It is noted that regardless of impact velocities, the stresses for Element A appear to give the highest magnitude, as compared to the Element C. This is attributed to the fact that Element A, which is located right at the tearing edge of the soft-catcher, experiences the highest amount of tearing resistance against the motion of wall debris.

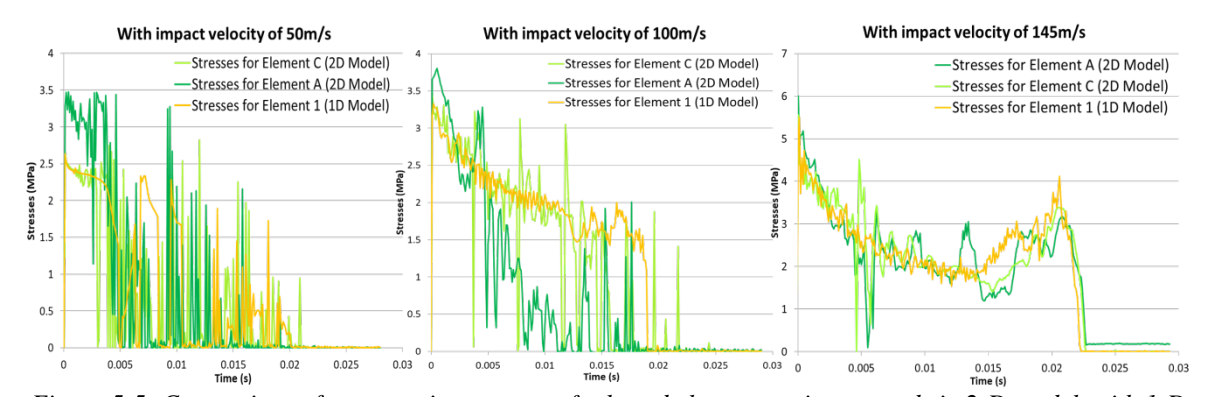


Figure 5-5: Comparison of compressive stresses of selected elements at impact ends in 2-D model, with 1-D model, under different impact velocities

The tensile stress development in 2-D model is one key aspect that differs from 1-D model. Figure 5-6 presents the contour plots of maximum principal (tensile) stresses for the 2-D models under impact velocity of 100 m/s, at debris penetration termination time (i.e. equivalent to the time when velocity of debris reaches zero). It is clearly seen that the region closer to the lateral support restraint develops higher tensile stresses. An opening can be seen to develop along the pre-defined tearing line. One would expect material nodes along the

interface to move in upward direction due to compressive stress waves propagating from the impact end. However, it is observed that the interface nodes of the soft-catcher region that undergoes compressive crushing are displaced downward. This can be attributed by the fact that Poisson Ratio for the foam materials in the numerical model are set at zero. With the increase of the Poisson Ratio, the opening along the tearing interface may reduce further. At this juncture, it is worth to note that the actual tearing failures of soft-catcher may eventually differ from Figure 5-6. Instead, the actual tearing failures are likely to localize within the overlying region, especially near the impact end of the soft-catcher.

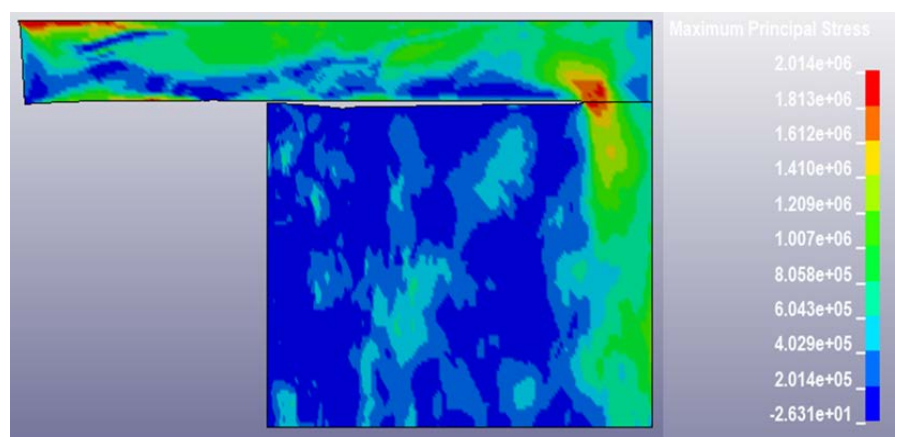


Figure 5-6: Contour plot of maximum principal stresses (tensile) for model with impact velocity of 100m/s (at time t = 0.022s)

## Reaction Forces at Boundary Support

Figure 5-7 shows that total resultant support forces are induced predominately in both negative-X and positive-Z direction along the lateral boundary support. The reaction forces in the negative-X direction indicate resistance against motion of wall debris, while the forces acting in the positive-Z direction imply that the foam materials near the lateral support restraint are subjected to tensile stresses during the impact duration, which is consistent with Figure 5-6. However, the build-up of positive-Z reaction forces may not be realistic to consider, as the bonding between the soft-catcher and the lateral containment wall is close to zero. It is interestingly noted that with lower impact velocities, the initial peak total reaction forces in both directions are found to be higher. This implies that the models with lower impact velocities are affected in greater extent, by the presence of tearing resistance. As time increases, reaction forces in both directions reduce to close zero.

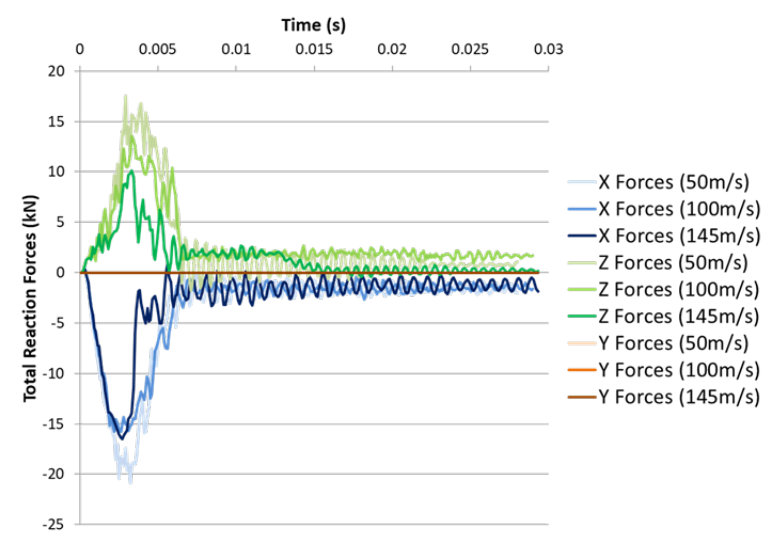


Figure 5-7: Total resultant reaction force-time histories plots for lateral support restraint

The height and width of the end boundary restraint in the 2-D model is 1.25 m and 0.010 m respectively. Figure 5-8 presents the total resultant support force-time histories of the end boundary restraint in X and Z-direction, for models with various impact velocities. The initial peak total reaction forces (i.e. due to induced elastic wave) in the 2-D model are found to be lower than the 1-D model. For the 2-D model with impact velocity of 145 m/s, higher total reaction forces of approximately 47 kN are observed at a later time. This is attributed by the plastic shock wave impacting against the end support. Nevertheless, it is worthwhile to note that this total reaction force of 47 kN is relatively close to the reaction force of 45.3 kN in the 1-D model. The reaction forces in the positive X-direction are mainly due to the subsequent reflections of remaining elastic waves.

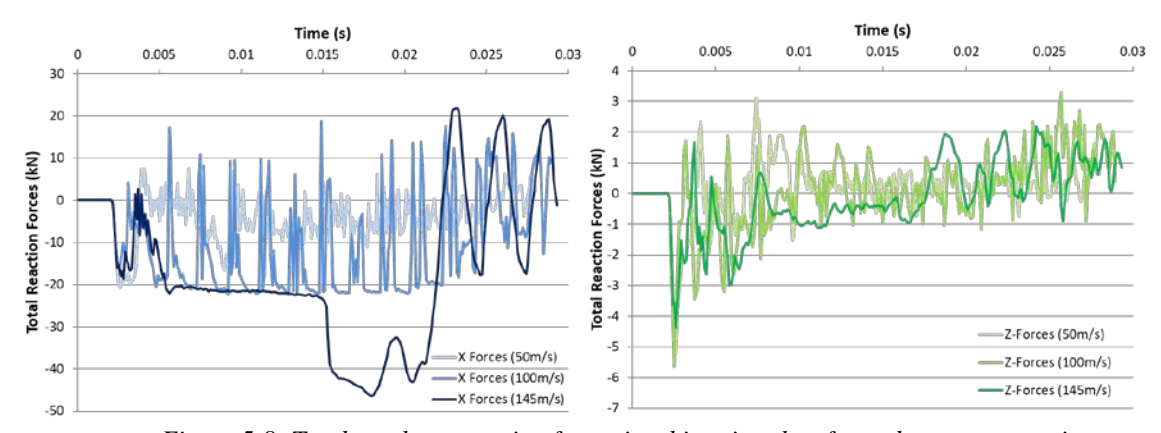


Figure 5-8: Total resultant reaction force-time histories plots for end support restraint

## 5.2. Sensitivity Study on Shear and Tensile Failure Stress

The failure envelope and definition of stress-based failure criterion are shown in Figure 5-9. The user-defined parameters include the NFLS, which refers to the tensile failure stress and the SFLS, which refers to the shear failure stress.

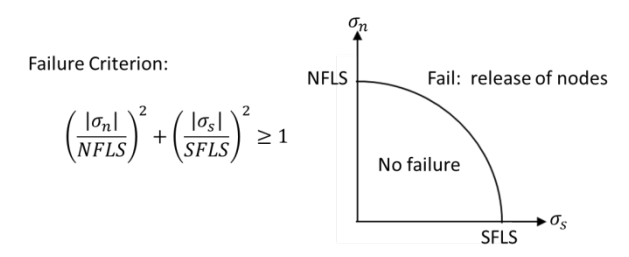


Figure 5-9: Failure criterion and failure envelope of tie-break connection

The effects of increasing shear (i.e. acting parallel to tearing interface) and tensile (i.e. acting normal to tearing interface) failure stresses of the soft-catcher on the overall interaction are evaluated, using the 2-D Model with an impact velocity of 100 m/s. A series of individual numerical analyses are run by either increasing the shear failure stress and keep the tensile failure stress fixed at base value, or vice versa. The base value for the shear and tensile failure stress is 1.86 MPa and 2.17 MPa respectively (See Table 2-1). The outcomes are plotted in Figure 5-10 and Figure 5-11. They clearly show that the shear resistance has greater influence on the resultant debris penetration distances and the peak compressive stresses induced at Element A, as compared to tensile resistance. This is reasonable since the shear stresses are acting in the direction similar to the debris motion. Apparently, the increases of either tensile or shear failure stresses indicate marginal influence over the development of peak total reaction forces at both lateral and end boundary support. This is mainly due to the fact that the magnitudes of reaction forces at boundary end primarily depend on the elastic yielding stress of the soft-catcher material.

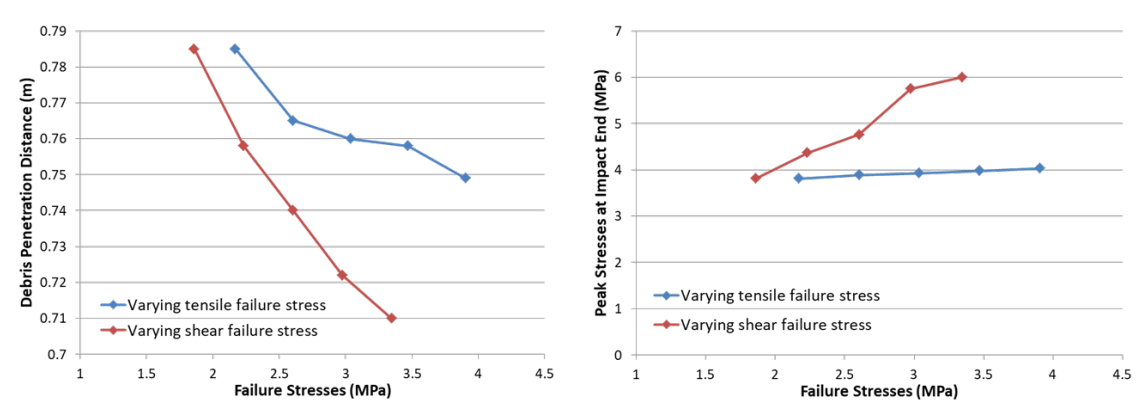


Figure 5-10: Debris penetration distances (left plot) and peak stresses of Element A (right plot), under the influence of varying tensile and shear failure stresses

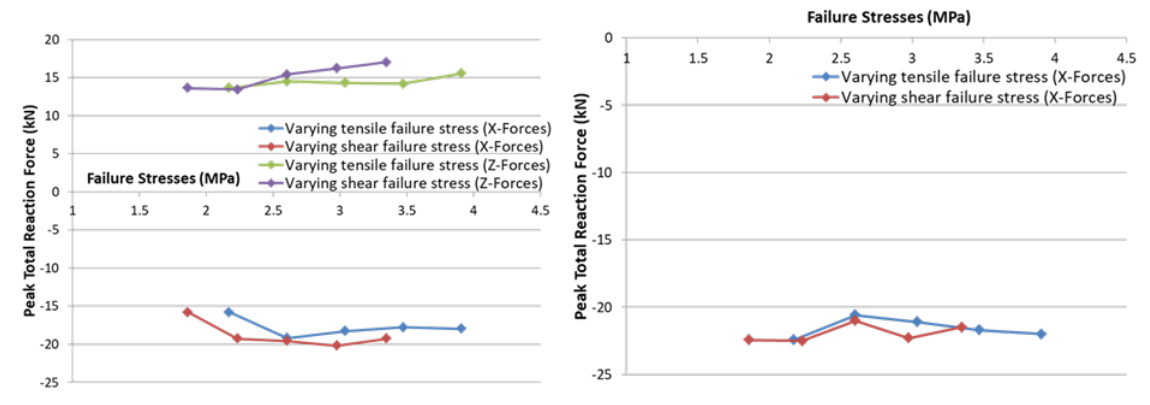


Figure 5-11: Peak total reaction forces at boundary supports, under the influence of varying tensile and shear failure stresses

## 6. Design Considerations for Soft-catcher

In order to facilitate the design of soft-catcher with a range of debris launch velocities, design charts are created with additional results obtained from various analytical and numerical models. The impact velocities of debris considered include 25 m/s, 50 m/s, 75 m/s, 100 m/s, 125 m/s and 145 m/s.

## What is the design length of soft-catcher?

Figure 6-1 presents the predictions of debris penetration distances in various models, over the range of debris launch velocities.

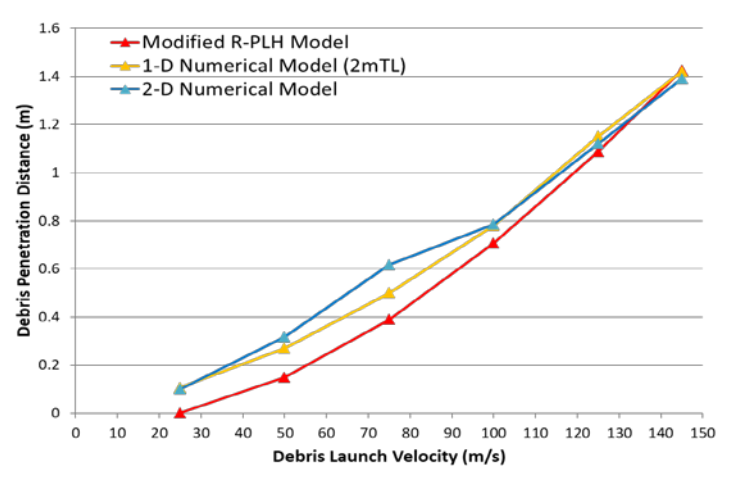


Figure 6-1: Debris penetration distance (m) over a range of debris launch velocities

With lower debris launch velocities, the Modified R-PLH Model predicts shorter debris penetration distances as compared to the numerical predictions. This is primarily due to the simplified approach of assuming an abrupt termination for the constant initial particle velocity when the shock wave terminates. The 2-D Model predicts longer debris penetration distances, especially for models with debris launch velocities of 50 m/s, 75 m/s and 100 m/s. This phenomenon can be possibly explained by the reduction of momentum transfers from the debris motion, due to drastic compressive stress oscillations experienced by the elements within the 2D model. However, at debris launch velocity of 145 m/s, the predictions from the all models are relatively close. With this observation, the design length of 2 m for the soft-catcher shall remain valid.

What are the impact stresses on the debris compared with the design strength of applied concrete and residual strength of damaged debris?

As illustrated in the left plot of Figure 6-2, both Modified-R-PLH Model and 1-D numerical models do not account for the increases in impact stresses on debris, due to material's failure resistances along the tearing interface. As such, the 2-D Model predicts a higher impact stresses, especially near the tearing interface along the front face of soft-catcher. The right plot of Figure 6-2 shows reduction in these differences when considering the average compressive stresses over the frontal face of soft-catcher in the 2-D model. Nevertheless, it is logical to see that as the debris launch velocity decreases; the impact stresses gradually reduce towards the yielding stress of the foam material.

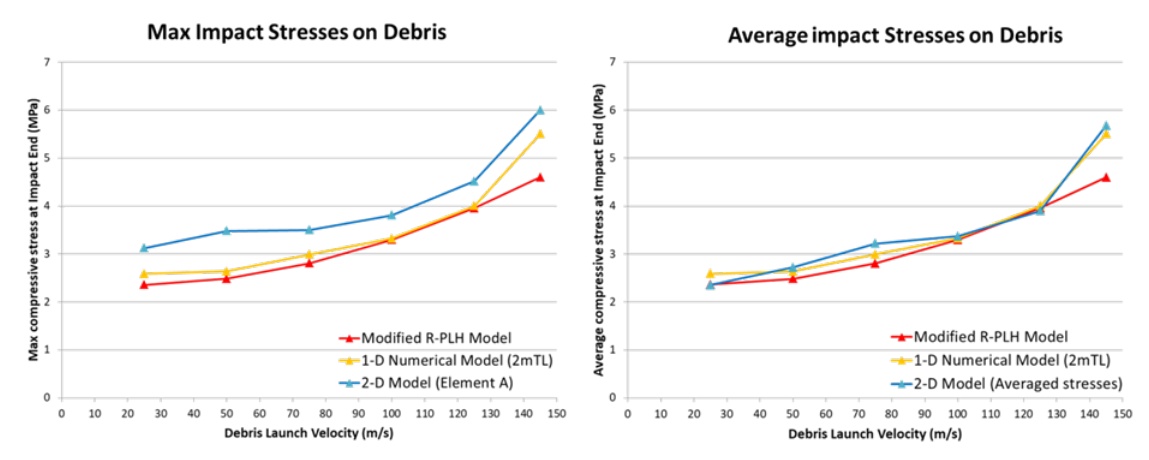


Figure 6-2: Predictions of maximum impact stresses (left plot) and average impact stresses (right plot) on debris over a range of launch velocities

From the introduction of this research work, it is mentioned that one of the guiding principles in choosing the appropriate material for the soft-catcher is to ensure no additional damage to the concrete debris during the soft-catching process. This implies that the impact stresses acting on the debris must not exceed the residual strength of concrete debris. In 2013, NTU carried out experimental investigation to quantify damage levels of chamfered concrete specimens, with cube size of 100mm, in accordance to crack-surface to volume ratio. The applied concrete strength is 35 MPa. Three different damage levels are defined and illustrated in Figure 6-3; 100% of peak load, 86.5% of peak load in post-peak regime and 73.1% of peak load in post-peak regime. The lowest ultimate strength (i.e. loading stress when concrete disintegrate) was found to be approximately 15 MPa. Based on the 2D model prediction with highest debris launch velocity of 145 m/s, the maximum impact stress reaches 6.0 MPa. This stress value is apparently lower than the observed lowest ultimate loading stresses of these concrete specimens. Furthermore, this maximum impact stress of 6.0 MPa is still within 20% of the compressive strength of 35 MPa.

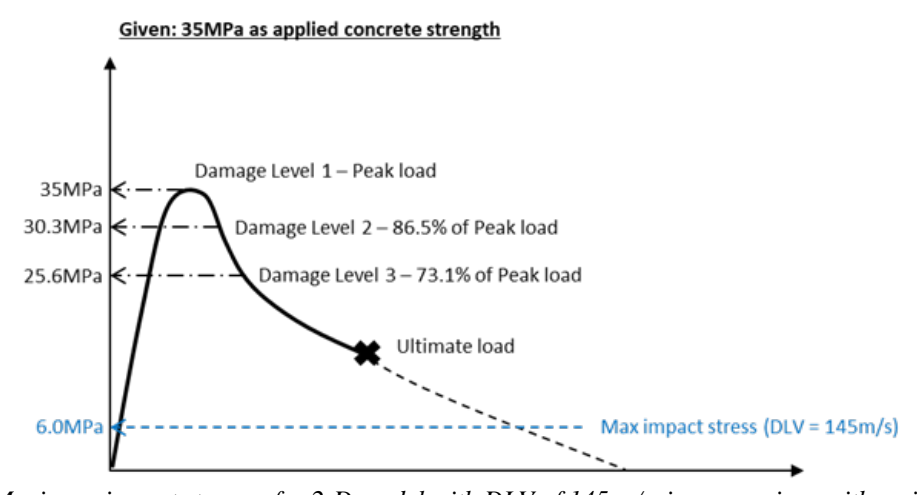


Figure 6-3: Maximum impact stresses for 2-D model with DLV of 145 m/s, in comparison with residual concrete strengths for damage level 1, 2 and 3 for an applied concrete strength of 35MPa

## What are the magnitudes of reaction forces at boundary supports of soft-catcher?

Figure 6-4 presents the total reaction forces at lateral and end boundary supports. It can be observed that as the debris launch velocity increases, lower peak total reaction forces are induced along the lateral boundary support. This can be associated to the increasing extent of

tearing failures along the pre-defined interface as the impact velocities increase. At the end boundary support, it appears that 1-D numerical models provide conservative predictions on the total reaction forces, as compared to the 2-D model.

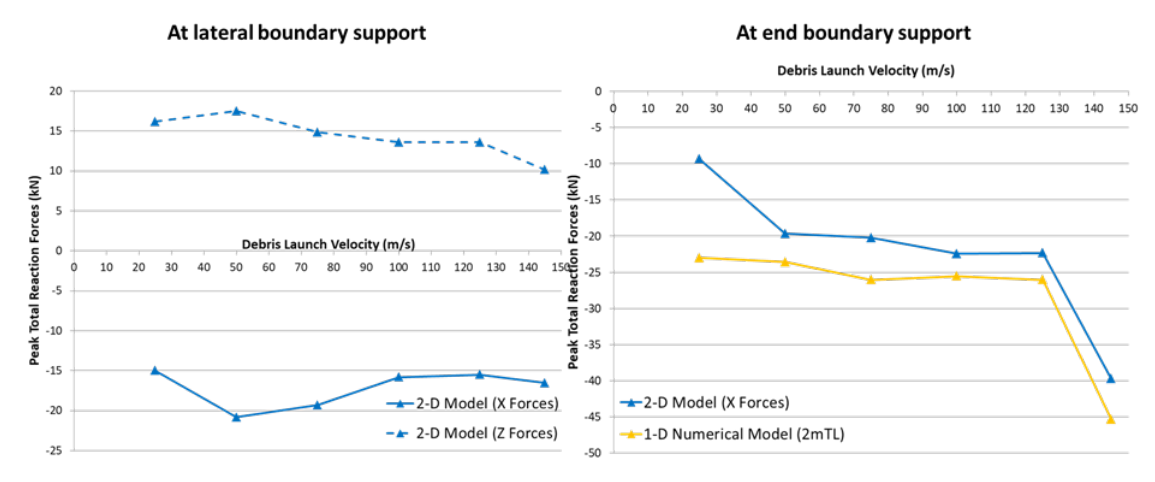


Figure 6-4: Predictions of total reaction forces at lateral boundary support (left plot) and at end boundary support (right plot) over a range of launch velocities

#### 7. Conclusions and Recommendations

This research studied the feasibility of using polymeric foam to soft-catch damaged concrete debris, arising from an internal explosion of an ammunition magazine structure. The resultant phenomena from the interaction between concrete debris and foam material are evaluated and translated into design considerations for the soft-catcher. A rigid polymethacrylimide foam material, known as Rohacell 110WF, is considered as the representative benchmark material for the soft-catcher. Initial efforts are focused on reviewing 1-D shock wave models, and formulating an improved analytical model (i.e. Modified R-PLH Model) to obtain preliminary design of soft-catcher, by predicting debris penetration distances, shock-induced stresses and strains within the foam materials. The improved model incorporates additional effects of induced elastic stress wave propagation. An impactor-target scenario involving single large wall debris is considered for evaluation. Different debris launch velocities are considered.

Verifications of analytical models are performed using 1-D numerical models with 20m target length in LS-DYNA. Two different debris velocity time response regimes (i.e. higher velocity time response regime; lower velocity time response regime) are identified from the debris velocity-time curves. The Modified-R-PLH Model shows improved predictions of debris deceleration, shock stresses and strains within the higher debris velocity time regimes. Realising that the presence of finite thickness of soft-catcher will have influences over debris penetration distances, the 1-D numerical model with target length of 2m (i.e. based on preliminary design length of soft-catcher) is constructed. The presence of end boundary condition at close proximity to the impact end of soft-catcher affects how debris decelerates within the lower velocity time regime. It also influences the plastic wave propagation, especially when higher impact velocities are involved. The consequences to design of soft-catcher using Modified-R-PLH Model are also discussed. The differences between the Modified R-PLH Model and numerical models in predicting the final debris penetration distance arise due to the assumption of how debris decelerates within the lower velocity time response regime. However, these differences generally reduce as impact velocity increases.

The impactor-target problem is escalated into a 2-D space domain, in which shear and tensile stress failures along a pre-defined tearing line are considered. Decreases in debris deceleration are observed during the late phase of debris penetration process in the 2-D models, as compared to both 1D analytical and numerical models, especially when the impact velocities are lower. 1D model generally under-predicts the impact stresses acting on the debris, as localised increases in these stresses are observed in 2-D model (i.e. at the tearing interface between the frontal edge of the soft-catcher and the debris). Reaction forces induced over the lateral and end boundary supports are also evaluated. Along the lateral boundary support, higher reaction forces (in particular, negative-X and positive-Z direction) are observed in 2-D model with lower impact velocities. Conversely, at the end boundary support, higher total reaction forces (in negative-X direction) due to plastic shock wave are obtained in the 2-D model with impact velocity of 145m/s. From the sensitivity study of tensile and shear failure stresses over the soft-catcher's responses (i.e. penetration depth, impact stresses on debris, support reaction forces), it is concluded that shear resistance plays an influential role over debris penetration distance and the peak compressive stresses induced over the impact end of soft-catcher. Finally, design charts are plotted to examine the changes in various softcatcher's design parameters over a range of debris launch velocity.

Moving forwards, possible areas for future research can include:

- *Improve prediction accuracy of Modified R-PLH Model*: The current approach is invalid to assume instantaneous drop of debris velocity to zero once the relative velocity of debris (i.e. respect to the particle elastic velocity) reaches zero. Instead, a linear decrease of debris velocity to reach zero velocity within the lower velocity time response regime can be considered, in which the rate of velocity decrease can follow the velocity gradient observed in the higher velocity regime.
- Use of continuum-based approach to model material failure mechanism: The current approach of pre-defining a tearing line to simulate the failure response of soft-catcher will not be realistic. Considering that tearing and crushing failures of soft-catcher can potentially occur within the overlying layer above the pre-defined tearing line, using element erosion techniques to simulate material failure will be more appropriate. The effect of different thicknesses of the overlying layer on the failure phenomenon can also be evaluated.
- Account for debris cloud effect: The current thesis simplifies the impact scenario by considering single large debris with size of the concrete wall. However, different shape coefficients, depending on the probable sizes of individual wall debris, can be evaluated to better represent a more realistic scenario, when debris cloud expands further. The numerical simulation can account for effects under multiple debris hits scenario in both spatial and time domain.
- Account for blast loading: The current thesis ignores the effect of blast loading onto the soft-catcher. However, numerical simulation can be carried out to account for the combined effects of blast and debris impact onto the soft-catcher. The blast pressure loading can be applied onto the frontal face of the soft-catcher, depending on the time of arrival for the blast wave to reach the soft-catcher. Under these additional surface loading, the foam material will be further densified, which can lead to higher initial impact stresses onto the debris and affect the overall debris penetration distance. Higher reaction forces can be expected to induce at the end support boundary
- Study effects of other foam material properties; other mechanical properties of soft-catcher (i.e. elastic modulus, yielding stress, initial density of foam etc.) on the overall material responses can also be investigated. This can eventually work towards delivering a more economical and effective solution for design consideration.

#### Acknowledgements

The author sincerely acknowledges the consistent efforts from the Thesis Assessment Committee from the Structural Mechanics Section in Faculty of Civil Engineering and Geosciences at Delft University of Technology, to provide valuable technical advices and guidance throughout the course of the research.

#### References

- [1] H. Lim, "Response of reinforced concrete slab to explosive," MSc thesis Delft University of Technology, 2005.
- [2] S. Arezoo, V. Tagarielli and N. Petrinic, "The mechanical response of Rohacell foams at different length scales," *J Master Sci*, pp. 6863 6870, 2011.
- [3] J. Van Doormaal, A. Dorr and F. R, "Debris Launch Velocity Program DLV," in 11th International Symposium on the Interaction of the Effects of Munitions with Structures, 2003.
- [4] A. Slobbe and J. Weerheijm, "Numerical Simulations of the Reinforced Concrete Kasun Structure under Internal Blast and Fragment Loading," TNO Draft Report, 2016.
- [5] S. Reid and C. Peng, "Dynamic Unaxial Crushing of Wood," *Int. J. Impact. Engrg Vol.* 19 Nos. 5-6, pp. 531-570, 1997.
- [6] P. Tan, S. Reid, J. Harrigan, Z. Zou and S. Li, "Dynamic compressive strength properties of aluminium foams. Part I Experimental data and observations," *Journal of the Mechanics and Physics of Solids* 53, pp. 2174-2205, 2005.
- [7] P. Tan, S. Reid and J. Harrigan, "On the Dynamic Mechanical Properties of Open-cell Metal Foams A re-assessment of the "simple-shock theory"," *Int. J. of Solids and Structures*, pp. 2744-2753, 2012.
- [8] Q. Li, I. Magkiriadis and J. Harrigan, "Compressive strain at the onset of densification of cellular solids," *Journal of Cellular Plastics*, vol. 42, pp. 371-392, 2006.
- [9] S. Pattofatto, I. Elnasri, H. Zhao, H. Tsitsiris, F. Hild and Y. Girard, "Shock enhancement of cellular structures under impact loading: Part II analysis," *Journal of the Mechanics and Physics of Solids*, vol. 55, pp. 2672-2686, 2007.
- [10] Z. Zheng, Z. Yu, C. Wang, S. Liao and Y. Liu, "Dynamic crushing of cellular materials: A unified framework of plastic shock wave models," *Int. J. of Impact Engrg*, vol. 53, pp. 29-43, 2013.
- [11] S. Jones and W. Rule, "On the optimal nose geometry for a rigid penetrator, including the effects of pressure-dependent friction," *Int. J. of Impact Engineering*, vol. 24, pp. 403-415, 2000.
- [12] X. Chen and Q. Li, "Deep penetration of a non-deformable projectile with different geometrical characteristics," *Int. J. of Impact Engrg*, vol. 27, pp. 619-637, 2002.
- [13] S. L. Lopatnikov, B. A. Gama, M. Jahirul Haque, C. Krauthauser, J. W. Gillespie Jr, M. Guden and I. W. Hall, "Dynamics of metal foam deformation during Taylor cylinder-Hopkinson bar impact experiment," *Composite Structures*, vol. 61, pp. 61-71, 2003.
- [14] Z. Zheng, Y. Liu, J. Yu and S. Reid, "Dynamic crushing of cellular materials: Continuum-based wave models for the transitional and shock modes," *Int. J. of Impact Engrg*, vol. 42, pp. 66-79, 2012.
- [15] J. Harrigan, S. Reid and A. Seyed Yaghoubi, "The correct analysis of shocks in cellular material," *Int. J. of Impact Engrg*, vol. 37, pp. 918-927, 2010.

- [16] L. J. Gibson and M. F. Ashby, Cellular solids structure and properties, 2nd Ed, Cambridge: Cambridge University Press, 1997.
- [17] "LS-DYNA Support," LSTC, [Online]. Available: http://www.dynasupport.com/.
- [18] LS-DYNA Keyword User's Manual Volume 2 Material Models LS-DYNA R8.0, Livermore Software Technology Corporation (LSTC).
- [19] LS-DYNA Keyword User's Manual Volume 1 LS-DYNA R8.0, Livermore Software Technology Corporation (LSTC).
- [20] D. Zenkert and M. Burman, "Tension, Compression and Shear Fatigue of a Closed Cell Foam," in *16th International Conference on Composite Materials*.

## Annex A – Derivation of Shape Coefficients $N_1$ and $N_2$

Figure A1 illustrates the schematic diagram of the resultant forces. In the case where debris penetrate into cellular material, p and f refer to the normal crushing force (due to stress enhancement) and frictional force respectively. The K represents strength index while the n represents strain hardening index.

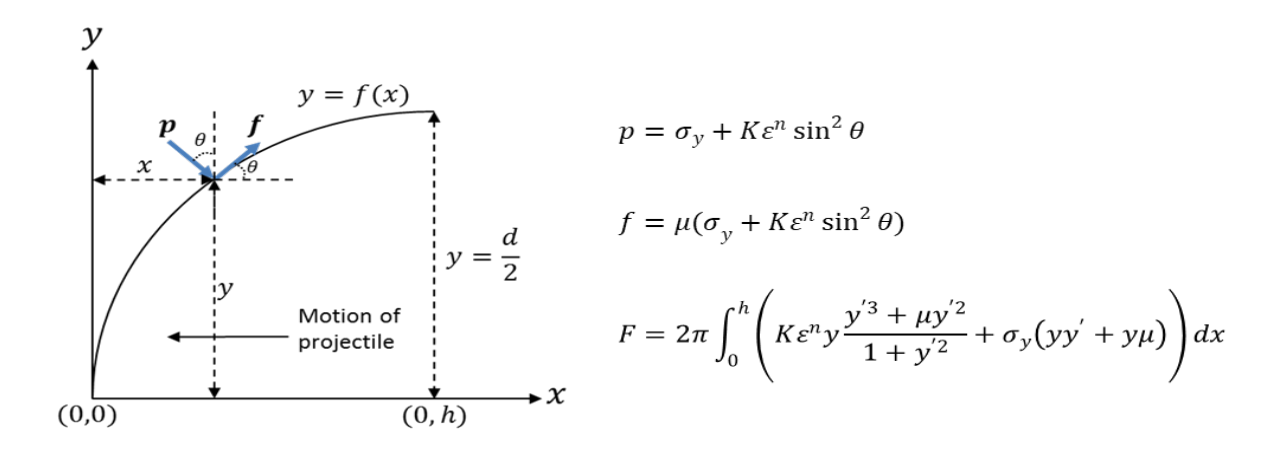


Figure A1: Cross-section for an axisymmetric projectile with hemispherical nose and equations describing the resultant forces, where F refers to the total force resisting the projectile motion

The equation of F presented in Figure A1 can be re-arranged to derive the two dimensionless parameters known as the shape coefficients  $N_1$  and  $N_1$ . Chen and Li in [11] had presented these coefficients into the penetration resistance, when formulating the equation of motion.

$$N_1 = 1 + \frac{8\mu}{d^2} \int_0^h y \, dx \qquad N_2 = N^* + \frac{8\mu}{d^2} \int_0^h \frac{yy'^2}{1 + y'^2} \, dx \qquad N^* = \frac{8}{d^2} \int_0^h \frac{yy'^3}{1 + y'^2} \, dx$$

With these shape coefficients, the crushing resistance of cellular material to debris penetration can be written as follows.

$$F_R = \frac{\pi d^2}{4} \left( N_1 \sigma_y + N_2 K \varepsilon^n \right)$$
 (For hemispherical nose shape of debris)  

$$F_R = wh \left( N_1 \sigma_y + N_2 K \varepsilon^n \right)$$
 (For flat nose shape of debris)

Where w and h are the width and height of the rectangular shape debris respectively. Note that in the case of debris with flat vertical nose, both  $N_1$  and  $N_1$  are equal to 1.

Note that the following derivations will include the notations of  $N_1$  and  $N_1$ 

#### (i) To derive Equation (2)

The jump conditions can be specified across the shock wave front, in function of time:

$$\begin{split} [\sigma] &= \sigma \big(\hat{\varepsilon}_B(t)\big) - \sigma_y \qquad [\varepsilon] = \varepsilon_B(t) - \varepsilon_Y = \hat{\varepsilon}_B(t) \\ [\sigma] &= \frac{\rho_o[v]^2}{[\varepsilon]} = \frac{\rho_o(v_B(t) - v_A(t))^2}{(\varepsilon_B(t) - \varepsilon_Y)} = \frac{\rho_o(v_B(t) - v_A(t))^2}{\hat{\varepsilon}_B(t)} \\ [v] &= v_B(t) - v_A(t) = \sqrt{\frac{1}{\rho_o}} \Big(\sigma(\hat{\varepsilon}_B) - \sigma_y\Big) \hat{\varepsilon}_B \\ \frac{d}{dt}(v_B - v_A) &= \frac{d}{dt} \Big(v_{Brelative}\Big) \\ &= \frac{1}{2} \Big(\frac{1}{\rho_o} \sigma(\hat{\varepsilon}_B) \hat{\varepsilon}_B - \frac{\sigma_y}{\rho_o} \hat{\varepsilon}_B\Big)^{-\frac{1}{2}} \Big(\frac{1}{\rho_o} \frac{d\sigma}{d\hat{\varepsilon}_B} \frac{d\hat{\varepsilon}_B}{dt} \hat{\varepsilon}_B + \frac{1}{\rho_o} \sigma(\hat{\varepsilon}_B) \frac{d\hat{\varepsilon}_B}{dt} - \frac{\sigma_y}{\rho_o} \frac{d\hat{\varepsilon}_B}{dt}\Big) \\ \frac{d}{dt}(v_B - v_A) &= \frac{d}{dt} \Big(v_{Brelative}\Big) = \frac{\frac{1}{2} \Big(\sigma'(\hat{\varepsilon}_B) + \frac{\sigma(\hat{\varepsilon}_B) - \sigma_y}{\hat{\varepsilon}_B}\Big) \hat{\varepsilon}_B}{\rho_o \sqrt{\frac{1}{\rho_o}} \frac{\sigma(\hat{\varepsilon}_B) - \sigma_y}{\hat{\varepsilon}_B}} \\ \end{split}$$

# (ii) To derive Equation (6)

Combining Equation (3) and (4):

$$-\frac{\sigma^*(\hat{\varepsilon}_B)}{m+\rho_o x(t)} = \frac{k(\hat{\varepsilon}_B)\dot{\hat{\varepsilon}_B}}{\rho_o \dot{x}} \quad \to \quad \frac{\rho_o}{m+\rho_o x(t)}\dot{x} = -\frac{k(\hat{\varepsilon}_B)}{\sigma^*(\hat{\varepsilon}_B)}\dot{\hat{\varepsilon}_B}$$

Integrating both side of equation gives the displacement function of plastic shock wave relative to the particle velocity in the pre-shock region.

$$\int_0^t \frac{\rho_o}{m + \rho_o x(t)} \dot{x} = -\int_0^t \frac{k(\hat{\varepsilon}_B)}{\sigma^*(\hat{\varepsilon}_B)} \dot{\hat{\varepsilon}_B}$$

$$\ln\left(\frac{m+\rho_ox(t=t)}{m+\rho_ox(t=0)}\right) = -\int_{\hat{\varepsilon}_B(t=0)}^{\hat{\varepsilon}_B(t=t)} \frac{k(\hat{\varepsilon}_B)}{\sigma^*(\hat{\varepsilon}_B)} d\hat{\varepsilon}_B$$

$$x(t) = \frac{m}{\rho_o} \left( exp\left( -\int_{\hat{\varepsilon}_o}^{\hat{\varepsilon}_B(t)} \frac{k(\hat{\varepsilon}_B)}{\sigma^*(\hat{\varepsilon}_B)} d\hat{\varepsilon}_B \right) - 1 \right)$$

Performing time derivative of the above expression gives relative shock wave speed:

$$\frac{d}{dt}x(t) = -\frac{mk(\hat{\varepsilon}_B)}{\rho_o \sigma^*(\hat{\varepsilon}_B)} \exp\left(-\int_{\hat{\varepsilon}_o}^{\hat{\varepsilon}_B(t)} \frac{k(\hat{\varepsilon}_B)}{\sigma^*(\hat{\varepsilon}_B)} d\hat{\varepsilon}_B\right) \frac{d\hat{\varepsilon}_B}{dt}$$

#### (iii) To derive Equation (7)

To formulate expression that relates the change in shock stresses and strains with respect to the changes in velocity jump:

Given that relative shock speed can be defined as:

$$\dot{x} = \sqrt{\frac{1}{\rho_o} \left( \frac{\sigma(\hat{\varepsilon}_B) - \sigma_y}{\hat{\varepsilon}_B} \right)}$$

Combining with Equation (6) gives

$$\sqrt{\frac{1}{\rho_o} \left( \frac{\sigma(\hat{\varepsilon}_B) - \sigma_y}{\hat{\varepsilon}_B} \right)} = -\frac{mk(\hat{\varepsilon}_B)}{\rho_o \sigma^*(\hat{\varepsilon}_B)} \exp\left( -\int_{\hat{\varepsilon}_o}^{\hat{\varepsilon}_B(t)} \frac{k(\hat{\varepsilon}_B)}{\sigma^*(\hat{\varepsilon}_B)} d\hat{\varepsilon}_B \right) \frac{d\hat{\varepsilon}_B}{dt}$$

$$\sqrt{\frac{1}{\rho_o} \left( \frac{\sigma(\hat{\varepsilon}_B) - \sigma_y}{\hat{\varepsilon}_B} \right)} = -\frac{mk(\hat{\varepsilon}_B)}{\rho_o \sigma^*(\hat{\varepsilon}_B)} \exp\left( -\int_{\hat{\varepsilon}_o}^{\hat{\varepsilon}_B(t)} \frac{k(\hat{\varepsilon}_B)}{\sigma^*(\hat{\varepsilon}_B)} \ d\hat{\varepsilon}_B \right) \frac{d\hat{\varepsilon}_B}{dt}$$

$$\sqrt{\frac{1}{\rho_o} \left( \frac{\sigma(\hat{\varepsilon}_B) - \sigma_y}{\hat{\varepsilon}_B} \right)} dt = -\frac{m}{\rho_o} f^*(\hat{\varepsilon}_B) d\hat{\varepsilon}_B; \quad f^*(\hat{\varepsilon}_B) = \frac{k(\hat{\varepsilon}_B)}{\sigma^*(\hat{\varepsilon}_B)} \exp\left( -\int_{\hat{\varepsilon}_o}^{\hat{\varepsilon}_B(t)} \frac{k(\hat{\varepsilon}_B)}{\sigma^*(\hat{\varepsilon}_B)} d\hat{\varepsilon}_B \right)$$

The dimensionless parameter  $f^*(\hat{\varepsilon}_B)$  is introduced to simplify the expression

$$\frac{\sqrt{\sigma(\hat{\varepsilon}_B) - \sigma_y}}{\sqrt{\rho_o \hat{\varepsilon}_B}} dt = -\frac{m}{\rho_o} f^*(\hat{\varepsilon}_B) d\hat{\varepsilon}_B$$

$$dt = -\frac{m\sqrt{\hat{\varepsilon}_B}}{\sqrt{\rho_o(\sigma(\hat{\varepsilon}_B) - \sigma_y)}} f^*(\hat{\varepsilon}_B) d\hat{\varepsilon}_B$$

Since the stress enhancement parameter can be defined as:

$$\alpha = \frac{K(\hat{\varepsilon}_o)^n}{\sigma_V}; \qquad \alpha = \frac{\rho_o[v]^2}{\hat{\varepsilon}_o} \qquad \to \qquad \rho_o = \frac{(\hat{\varepsilon}_o)^n K}{(V_o - V_A)^2} \hat{\varepsilon}_o$$

Therefore, it follows that:

$$dt = -m \frac{\sqrt{\hat{\varepsilon}_B} f^*(\hat{\varepsilon}_B)}{\sqrt{\frac{(\hat{\varepsilon}_o)^n K}{(V_o - v_A)^2}} \hat{\varepsilon}_o (\sigma(\hat{\varepsilon}_B) - \sigma_y)} d\hat{\varepsilon}_B$$

Integrating both side of equation gives:

$$t = -T \int_{\hat{\varepsilon}_o}^{\hat{\varepsilon}_B(t)} \frac{f^*(\hat{\varepsilon}_B) \sqrt{\sigma_y \hat{\varepsilon}_B}}{\sqrt{\alpha \hat{\varepsilon}_o \left(\sigma(\hat{\varepsilon}_B) - \sigma_y\right)}} d\hat{\varepsilon}_B$$

 $f^*(\hat{\varepsilon}_B)$  is the dimensionless function, T is the characteristic time parameter and  $\alpha$  is the stress-enhancement parameter.

$$f^*(\hat{\varepsilon}_B) = \frac{k(\hat{\varepsilon}_B)}{\sigma^*(\hat{\varepsilon}_B)} \exp\left(-\int_{\hat{\varepsilon}_O}^{\hat{\varepsilon}_B(t)} \frac{k(\hat{\varepsilon}_B)}{\sigma^*(\hat{\varepsilon}_B)} \ d\hat{\varepsilon}_B\right) \ ; \ T = \frac{m(V_O - v_{A_{initial}})}{\sigma_y} \ ; \ \alpha = \frac{K(\hat{\varepsilon}_O)^n}{\sigma_y}$$

$$\hat{\varepsilon}_o = \left(\frac{\rho_o (V_o - v_{A_{initial}})^2}{K}\right)^{\frac{1}{n+1}}$$

## (iv) To derive Equation (8)

To solve for Equation (8), there is need to evaluate and solve the integral of  $f^*(\hat{\varepsilon}_B)$  With the following relationship:

$$\sigma'(\hat{\varepsilon}_B) = n \frac{\sigma(\hat{\varepsilon}_B) - \sigma_y}{\hat{\varepsilon}_B} \rightarrow k(\hat{\varepsilon}_B) = \frac{n+1}{2n} \sigma'(\hat{\varepsilon}_B) = q \sigma'(\hat{\varepsilon}_B)$$

$$\sigma'(\hat{\varepsilon}_B) = n K(\hat{\varepsilon}_B)^{n-1}$$

$$\sigma^*(\hat{\varepsilon}_B) = N_1(\sigma_y) + N_2 K(\hat{\varepsilon}_B)^n$$

The dimensionless function  $f^*(\hat{\varepsilon}_R)$  can be evaluated as follows.

$$f^{*}(\hat{\varepsilon}_{B}) = \frac{k(\hat{\varepsilon}_{B})}{\sigma^{*}(\hat{\varepsilon}_{B})} \exp\left(-\int_{\hat{\varepsilon}_{o}}^{\hat{\varepsilon}_{B}(t)} \frac{k(\hat{\varepsilon}_{B})}{\sigma^{*}(\hat{\varepsilon}_{B})} d\hat{\varepsilon}_{B}\right)$$

$$f^{*}(\hat{\varepsilon}_{B}) = \frac{q\sigma'(\hat{\varepsilon}_{B})}{N_{1}(\sigma_{y}) + N_{2}K(\hat{\varepsilon}_{B})^{n}} \exp\left(-\int_{\hat{\varepsilon}_{o}}^{\hat{\varepsilon}_{B}(t)} \frac{q\sigma'(\hat{\varepsilon}_{B})}{\sigma^{*}(\hat{\varepsilon}_{B})} d\hat{\varepsilon}_{B}\right)$$
With  $\alpha = \frac{K(\hat{\varepsilon}_{o})^{n}}{\sigma_{y}} \rightarrow \sigma_{y} = \frac{K(\hat{\varepsilon}_{o})^{n}}{\alpha}$ 

$$f^{*}(\hat{\varepsilon}_{B}) = \frac{qnK(\hat{\varepsilon}_{B})^{n-1}}{N_{1}\frac{K(\hat{\varepsilon}_{o})^{n}}{\alpha} + N_{2}K(\hat{\varepsilon}_{B})^{n}} \left(\exp(-q)\left(\exp\left(\frac{\ln(\sigma^{*}(\hat{\varepsilon}_{B})) - \ln(\sigma^{*}(\hat{\varepsilon}_{o}))}{N_{2}}\right)\right)\right)$$

$$f^{*}(\hat{\varepsilon}_{B}) = \frac{qn\alpha(\hat{\varepsilon}_{B})^{n-1}}{(\hat{\varepsilon}_{o})^{n}\left(N_{1} + N_{2}\alpha\left(\frac{\hat{\varepsilon}_{B}}{\hat{\varepsilon}_{o}}\right)^{n}\right)} \left(\exp(-q)\left(\exp\left(\ln\left(\frac{\sigma^{*}(\hat{\varepsilon}_{B})}{\sigma^{*}(\hat{\varepsilon}_{o})}\right)\right)\right)\right)$$

$$f^{*}(\hat{\varepsilon}_{B}) = \frac{qn\alpha(\hat{\varepsilon}_{B})^{n-1}}{(\hat{\varepsilon}_{o})^{n}\left(N_{1} + N_{2}\alpha\left(\frac{\hat{\varepsilon}_{B}}{\hat{\varepsilon}_{o}}\right)^{n}\right)} \left(\frac{N_{1}(K(\hat{\varepsilon}_{o})^{n}) + N_{2}K(\hat{\varepsilon}_{B})^{n}}{\alpha} + N_{2}K(\hat{\varepsilon}_{o})^{n}\right)^{-q}$$

$$f^{*}(\hat{\varepsilon}_{B}) = \frac{qn\alpha(\hat{\varepsilon}_{B})^{n-1}}{(\hat{\varepsilon}_{o})^{n}\left(N_{1} + N_{2}\alpha\left(\frac{\hat{\varepsilon}_{B}}{\hat{\varepsilon}_{o}}\right)^{n}\right)} \frac{(N_{1} + N_{2}\alpha)^{q}}{\alpha} \left(\frac{N_{1} + N_{2}\alpha(\hat{\varepsilon}_{B})^{n}}{\hat{\varepsilon}_{a}}\right)^{q}\right)^{q}$$

$$f^*(\hat{\varepsilon}_B) = \frac{nq\alpha(N_1 + N_2\alpha)^q \left(\frac{\hat{\varepsilon}_B}{\hat{\varepsilon}_o}\right)^{n-1}}{\hat{\varepsilon}_o \left(N_1 + N_2\alpha \left(\frac{\hat{\varepsilon}_B}{\hat{\varepsilon}_o}\right)^n\right)^{q+1}}$$

Substitute the above expression of  $f^*(\hat{\varepsilon}_B)$  into the Equation (7)

$$t = -\frac{Tnq}{\hat{\varepsilon}_o} (N_1 + N_2 \alpha)^q \sqrt{\alpha} \int_{\hat{\varepsilon}_o}^{\hat{\varepsilon}_B(t)} \frac{\left(\frac{\hat{\varepsilon}_B}{\hat{\varepsilon}_o}\right)^{n-1} \sqrt{\sigma_y \hat{\varepsilon}_B}}{\left(N_1 + N_2 \alpha \left(\frac{\hat{\varepsilon}_B}{\hat{\varepsilon}_o}\right)^n\right)^{q+1} \sqrt{\hat{\varepsilon}_o \left(\sigma(\hat{\varepsilon}_B) - \sigma_y\right)}} d\hat{\varepsilon}_B$$

Since 
$$\sqrt{\alpha} = \left(\frac{K(\hat{\varepsilon}_o)^n}{\sigma_y}\right)^{\frac{1}{2}}$$

$$t = -\frac{Tnq}{\hat{\varepsilon}_o} (N_1 + N_2 \alpha)^q \frac{K^{\frac{1}{2}} (\hat{\varepsilon}_o)^{\frac{n}{2}}}{\sigma_y^{\frac{1}{2}}} \int_{\hat{\varepsilon}_o}^{\hat{\varepsilon}_B(t)} \frac{\left(\frac{\hat{\varepsilon}_B}{\hat{\varepsilon}_o}\right)^{n-1} \left(\frac{\hat{\varepsilon}_B}{\hat{\varepsilon}_o}\right)^{\frac{1}{2}} \sigma_y^{\frac{1}{2}}}{\left(N_1 + N_2 \alpha \left(\frac{\hat{\varepsilon}_B}{\hat{\varepsilon}_o}\right)^n\right)^{q+1} \sqrt{\left(\sigma(\hat{\varepsilon}_B) - \sigma_y\right)}} d\hat{\varepsilon}_B$$

The time function can be further simplified into:

$$t = -\frac{Tnq}{\hat{\varepsilon}_o} (N_1 + N_2 \alpha)^q \int_{\hat{\varepsilon}_o}^{\hat{\varepsilon}_B(t)} \frac{\left(\frac{\hat{\varepsilon}_B}{\hat{\varepsilon}_o}\right)^{\frac{n-1}{2}}}{\left(N_1 + N_2 \alpha \left(\frac{\hat{\varepsilon}_B}{\hat{\varepsilon}_o}\right)^n\right)^{q+1}} d\hat{\varepsilon}_B$$

Solving the integral of the above equation will eventually give the final expression for the time function as follows.

$$t = \frac{T}{N_1} \left( 1 - \left( \frac{N_1 + N_2 \alpha}{N_1 \left( \frac{\hat{\varepsilon}_B}{\hat{\varepsilon}_a} \right)^{-n} + N_2 \alpha} \right)^q \right)$$

## (v) To derive Equation (9)

Equation (8) can be re-arranged to give

$$1 - \frac{t(N_1)}{T} = \left(\frac{N_1 + N_2 \alpha}{N_1 \left(\frac{\hat{\varepsilon}_B}{\hat{\varepsilon}_o}\right)^{-n} + N_2 \alpha}\right)^q$$

$$N_1 \left(\frac{\hat{\varepsilon}_B}{\hat{\varepsilon}_o}\right)^{-n} + N_2 \alpha = \frac{N_1 + N_2 \alpha}{\left(1 - \frac{t(N_1)}{T}\right)^{\frac{1}{q}}}$$

$$\left(\frac{\hat{\varepsilon}_B}{\hat{\varepsilon}_o}\right)^{-n} = \frac{N_1 + N_2 \alpha}{N_1 \left(1 - \frac{t(N_1)}{T}\right)^{\frac{1}{q}}} - \frac{N_2 \alpha}{N_1}$$

$$\hat{\varepsilon}_B = \hat{\varepsilon}_B(t) = \hat{\varepsilon}_o \left( \frac{1}{N_1} \left( \frac{N_1 + N_2 \alpha}{\left(1 - \frac{t(N_1)}{T}\right)^{\frac{1}{q}}} - N_2 \alpha \right) \right)^{-\frac{1}{n}}$$

## (vi) To derive Equation (10)

Given the following definitions

$$\sigma(\hat{\varepsilon}_B) = \sigma_y + K(\hat{\varepsilon}_B)^n \; ; \; K = \frac{\alpha \sigma_y}{(\hat{\varepsilon}_O)^n}$$

The shock stress function can be derived as follows.

$$\sigma(\hat{\varepsilon}_B) = \sigma_y + \frac{\alpha \sigma_y}{(\hat{\varepsilon}_o)^n} (\hat{\varepsilon}_B)^n$$

$$\sigma(t) = \sigma_y + \frac{\alpha \sigma_y}{(\hat{\varepsilon}_o)^n} \left( \hat{\varepsilon}_o \left( \frac{1}{N_1} \left( \frac{N_1 + N_2 \alpha}{\left( 1 - \frac{t(N_1)}{T} \right)^{\frac{1}{q}}} - N_2 \alpha \right) \right)^{-\frac{1}{n}} \right)^n$$

$$\sigma(\hat{\varepsilon}_B) = \sigma_B(t) = \sigma_y \left( 1 + \alpha \left( \frac{1}{N_1} \left( \frac{N_1 + N_2 \alpha}{\left( 1 - \frac{t(N_1)}{T} \right)^{\frac{1}{q}}} - N_2 \alpha \right) \right)^{-1} \right)$$

#### (vii) To derive Equation (11)

The velocity functions of debris and crushed material, relative to the particle velocity of material within the pre-shocked region can be formulated from the Rankine-Hugoniot jump conditions.

Given the definitions of velocity jump  $[v] = \sqrt{\frac{1}{\rho_o}[\sigma][\varepsilon]}$  and considering the various jump conditions

$$\begin{split} [v] &= v_B(t) - v_A(t) = v_{Brelative} & [\sigma] = K(\hat{\varepsilon}_B)^n \\ v_{Brelative} &= \left(\frac{1}{\rho_o}K(\hat{\varepsilon}_B)^n\hat{\varepsilon}_B\right)^{\frac{1}{2}} \end{split}$$

Since the stress enhancement parameter can be defined as:

$$\alpha = \frac{K(\hat{\varepsilon}_o)^n}{\sigma_v}; \qquad \alpha = \frac{\rho_o[v]^2}{\hat{\varepsilon}_o} \qquad \to \qquad \rho_o = \frac{(\hat{\varepsilon}_o)^{n+1}K}{(V_o - v_A)^2}$$

Therefore, it follows that

$$v_{B_{relative}} = \left(\frac{(V_o - v_A)^2}{(\hat{\varepsilon}_o)^{n+1} K} K(\hat{\varepsilon}_B)^n \hat{\varepsilon}_B\right)^{\frac{1}{2}}$$

$$v_{B_{relative}} = (V_o - v_A) \left( \frac{1}{(\hat{\varepsilon}_o)^{n+1}} (\hat{\varepsilon}_B)^{n+1} \right)^{\frac{1}{2}}$$

Substitute the Equation (9) into the above equation to give the final expression for the relative velocity-time function of the debris and crushed material

$$v_{B_{relative}} = \left(V_o - v_{A_{initial}}\right) \left(rac{1}{N_1} \left(rac{N_1 + N_2 lpha}{\left(1 - rac{t(N_1)}{T}
ight)^{rac{1}{q}}} - N_2 lpha
ight)
ight)^{-q}$$

## (viii) To derive Equation (12)

Similarly, the relative velocity of shock wave front can be formulated from the Rankine-Hugoniot jump conditions.

Given the definitions of velocity jump  $\dot{x} = \sqrt{\frac{1}{\rho_o} \frac{[\sigma]}{[\varepsilon]}}$  and substitute with the following expressions

$$[\sigma] = K(\hat{\varepsilon}_B)^n \qquad [\varepsilon] = \varepsilon_B(t) - \varepsilon_y = \hat{\varepsilon}_B(t) \qquad \rho_o = \frac{(\hat{\varepsilon}_o)^{n+1} K}{(V_o - V_A)^2}$$

$$\dot{x} = (V_o - V_A) \left(\frac{(\hat{\varepsilon}_B)^n}{(\hat{\varepsilon}_o)^{n+1} \hat{\varepsilon}_B}\right)^{\frac{1}{2}}$$

Substitute the Equation (9) into the above equation to give the final expression for the relative velocity-time function of the shock wave front

$$\dot{x} = \frac{V_o - v_{A_{initial}}}{\hat{\varepsilon}_o} \left( \frac{1}{N_1} \left( \frac{N_1 + N_2 \alpha}{\left(1 - \frac{t(N_1)}{T}\right)^{\frac{1}{q}}} - N_2 \alpha \right) \right)^{q-1}$$

Annex C – List of model assumptions and what to verify in 1-D numerical analyses

#### 1-D Numerical Analyses Modified-R-PLH Model **R-PLH Model** Single rigid debris Single rigid debris impact impact 1-D stress wave 1-D stress wave propagation propagation Homogeneity of Homogeneity of material along impact material along impact direction direction Effect of end boundary in Infinite thickness of Infinite thickness of 2mTL model foam foam Same velocity for Same velocity for crushed particles in crushed particles in **→** To verify plastic zone and debris plastic zone and debris Shock-induced strain Uniform distribution of → To verify and stress directly shock-induced stresses behind wave front behind wave front Material reaches Material reaches To verify yielding stress in yielding stress in uncrushed zone uncrushed zone Zero strain for material Material in uncrushed zone To verify in uncrushed zone reaches elastic yield strain Zero particle velocity Non-zero particle velocity ➤ To verify due to elastic waves due to elastic waves

## **Annex D – Numerical Modeling Information**

#### **Material Model Validation:**

The quasi-static material cell test is performed using explicit solver in LS-DYNA. The Lagrangian solid elements (eight-node solid element) with ELFORM = EQ. 1 (under-integrated constant stress solid element) is used to model the cell. Figure D1 shows the single brick element constructed for the cell test.

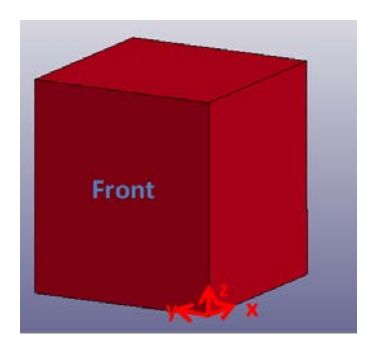


Figure D1: Single brick (1-point integration) element for cell test

The material model MAT\_63 is an isotropic crushable foam model that responds mainly in one-dimensional manner. The tensile behaviour assumes a perfectly-plastic response with a user-defined tensile cut-off stress value. The unloading is assumed to be elastic, which will reach this cut-off stress value, before reloading to follow the material's stress-strain curve. The material compressive constitutive relationship, in the form of stress versus volumetric strain, will be incorporated via DEFINE\_CURVE card. The volumetric strain  $\gamma$  is defined as 1 minus relative volume V. The relative volume refers to the ratio of the current volume over the initial volume of the element. Figure D2 illustrates the material's constitutive curve (as input curve) and various input parameters for MAT 63.

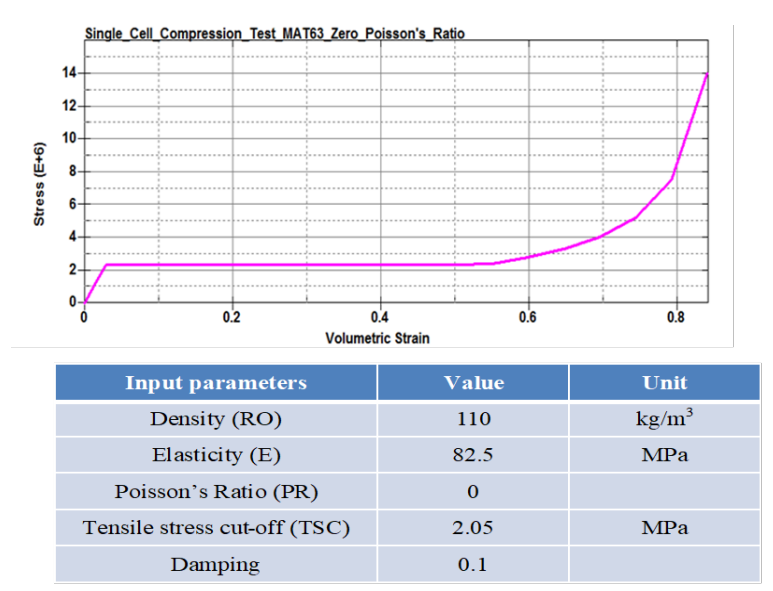


Figure D2: Material constitutive curve and various parameters defined in LS-DYNA

The compressive loadings to the element are applied via PRESCRIBED\_MOTION\_SET. The top four nodes are assigned with prescribed displacement at various loading rates, ranging from 0.001m/s to 145m/s.

#### **1-D Numerical Models**

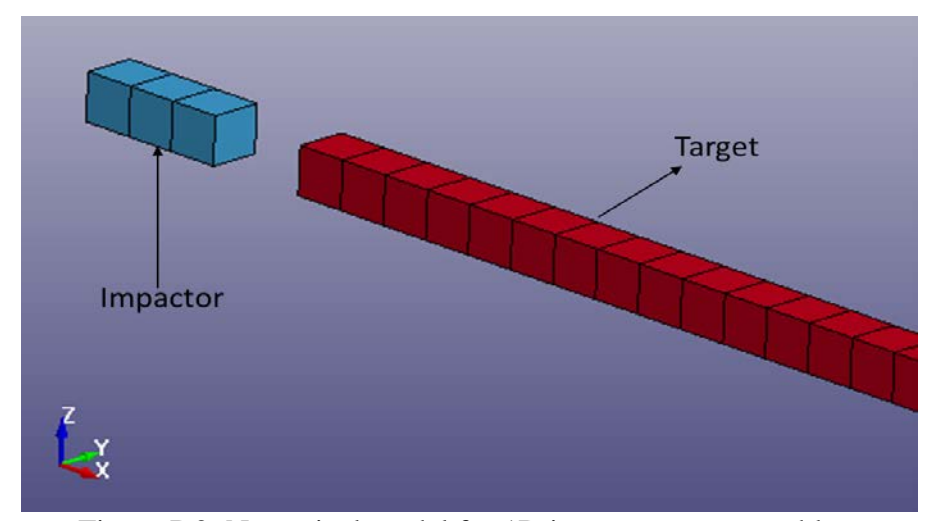


Figure D3: Numerical model for 1D impactor-target problem

#### **Element formulation:**

Both debris and soft-catcher are modelled using solid constant stress elements with single integration point (i.e. element formulation type: ELFORM 1), to lower the risk of numerical instabilities.

## **Hourglass control:**

To avoid negative volume errors in soft material (i.e. foam), HOURGLASS control is incorporated with formulation type 2 (Flanagan-Belytschko viscous form), as recommended (by LS-DYNA online support).

#### Contact algorithm:

The ability for numerical models to predict reasonably well the responses of debris and softcatcher depends very much on the modelling accuracy of the contact interface. It is always desirable to avoid unnecessary initial penetrations between the contact surfaces. CONTACT\_AUTOMATIC\_SURFACE\_TO\_SURFACE is selected as the contact type option, considering that the contact area between the debris and soft-catcher is relatively large. It is also preferable to use segment-based contact since the interaction between different parts involves sharp corners. For the reason that the differences in the material stiffness between concrete and foam can be considerably large, the scale factors on slave penalty stiffness (for debris) and master penalty stiffness (for soft-catcher) are adjusted to 0.1 and 10 respectively. Recognising that large deformations of elements (i.e. soft-catcher) under effects of moderate to high impact velocity will likely to cause numerical errors due to element inversions, CONTACT\_INTERIOR card with crush activation thickness factor of 0.1 (default) and contact interior type 1 (i.e. for uniform compression) are assigned for softcatcher. Furthermore, an optional card (SOFT=2), which is meant for segment-based contact, is activated in the CONTACT card. This option is recommended for contact interface involving soft materials such as foam material.

## <u>Timestep control:</u>

The CONTROL\_TIMESTEP card is included to reduce the timestep scaling factor (TSSFAC) from the default value of 0.9 to 0.1. In doing so, the critical time-steps in the analyses are reduced and that the problem of contact penetration errors, especially in the cases when higher impact velocities are involved, can be avoided. Though, it is noted that the runtime taken to complete the numerical analyses generally increases.

## Others:

The boundary conditions are specified via BOUNDARY\_SPC\_SET cards. The moving velocities of debris are incorporated through INITIAL\_VELOCITY card. DATABASE-NODFOR and DATABASE-NODAL-FORCE-GROUP cards are included to enable processing of the global forces from the boundary conditions.